Effects of iron substitution and anti-site disorder on crystal structures, vibrational, optical and magnetic properties of double perovskites $Sr_2(Fe_{1-x}Ni_x)TeO_6$

Asmaa ZARAQ[1, 2*], Duncan H. GREGORY[2], Brahim ORAYECH[3], Josu M. IGARTUA[4], Abdeslam EL BOUARI[5], James D. EALES[6], Paul A. BINGHAM[6], and Thorsten M. GESING[1,7]

[1]University of Bremen, Institute of Inorganic Chemistry and Crystallography, Bremen, Germany,

[2]WestCHEM School of Chemistry, University of Glasgow, Joseph Black Building, Glasgow G12 8QQ, United Kingdom,

[3]Maxam, Technology Center Energetic Materials, Carretera N-623 km 28. 09141Quintanilla Sobresierra. Burgos, Spain,

[4]Universidad del País Vasco/Euskal Herriko Unibertsitatea UPV/EHU: Leioa, Bizkaia, España,

[5]Laboratory of Physical-Chemistry, Materials and Catalysis, Department of Chemistry, Faculty of Sciences Ben M'Sik, University Hassan II of Casablanca, Casablanca, Morocco,

[6]Materials and Engineering Research Institute, Sheffield Hallam University, City Campus, Howard Street, Sheffield, S1 1WB, United Kingdom,

[7]University of Bremen, MAPEX Center for Materials and Processes, Bremen, Germany.

*Corresponding author: assmaa.zaraq@gmail.com,
zaraq@uni-bremen.de,
+49 (0)421 218 63141

#ORCID:
AZ: 0000-0003-1017-8251
BO: 0000-0003-3707-7645
JMI: 0000-0001-7983-5331
AE: 0000-0002-4960-904X
DHG: 0000-0002-4585-3280
JDE: 0000-0001-6914-0341
PAB: 0000-0001-6017-0798
TMG:0000-0002-4119-2219

Abstract

The double-perovskite series, $Sr_2(Fe_{1-x}Ni_x)TeO_6$ (x = *0*, *0.25*, *0.50*, *0.75*, and *1*) has been synthesized in polycrystalline form by solid-state reaction at 1300 K in air. Their crystal structures were probed by powder X-ray diffraction at room temperature. Rietveld analysis revealed that all samples crystallize in the monoclinic space group *I*2/*m*. The double-perovskite structures ideally contain two alternating types of octahedra $(Fe/Ni)^{2d}O_6$ and $(Te)^{2a}O_6$, tilted in the system ($a^-a^-c^0$). However, the refinements have shown a complex distribution of all three cations over the two available octahedral sites ; *2d (½, ½, 0)* and *2a (0, 0, 0)*. Raman spectroscopy further complements the obtained results, by revealing a tiny increase of the wavenumber of some Raman modes when Fe is substituted by Ni. The

optical characteristics of the series were determined by fitting diffuse reflectance UV/Vis spectra enabling the optical band gaps to be derived from Tauc method and Derivation of Absorption Spectra Fitting (DASF) techniques. Analyses of the obtained ^{57}Fe Mössbauer hyperfine parameters at room temperature of samples with compositions *x = 0, 0.25, 0.50* and *0.75* reveal the presence of Fe^{3+} in high-spin state with an anti-site disorder of Fe-Ni-Te cations in distorted octahedral environments (site *2d* and *2a*). The results show that significant correlations exist between the crystal structures and physical properties of double perovskites containing *B* site transition elements of different charge and size. Temperature-dependent magnetic susceptibility data show magnetic transitions below 40 (1) K (38 (1) K, 31(1) K, 25 (1) K, 20(1) K, and 35(1) K for *x = 0, 0.25, 0.50, 0.75*, and *1*, respectively. A divergence between FC and ZFC curves for all compositions has been observed. The results, show that the ground state of the doped materials might be spin glasses or magnetically ordered.

Keywords

double-perovskite oxide, X-ray powder diffraction, Rietveld method, octahedral distortion, Raman, optical properties, Mössbauer spectroscopy, magnetism.

1. INTRODUCTION

Over the past years, transition metal double-perovskite (DP) crystal structures have attained great interest due to their ability to crystallize in all seven crystal systems, depending on the elements *A* and *B* (as defined for oxide perovskites ABO_3; *A* = 12-coordinate cation, *B* = 6-coordiate cation), as well as the ordering of these cations on the octahedral sites and the synthesis method employed. [1-3]. This leads to an enormous variety of physical properties which explains why perovskite is one of the dominant basic structures for a host of materials with industrial and scientific applications. Among many, these include half-metallicity and ferromagnetism for spintronics [4, 5], semiconductivity for photocatalytic water oxidation [6, 7] or piezo- and ferroelectricity for photovoltaic solar cells [8, 9]. It is not surprising that perovskites and related superstructures continue to be attractive for research over many decades of study.

As the variety of properties and applications of DPs comes from a combination of strongly correlated components such as *3d* elements, the DP structure "$A_2BB'O_6$" is highly dependent on the arrangement of those elements in the *B* sites [10,11]. In general, three factors affect the arrangement of B-site cations; ionic charge, ionic size, and electronic configuration [12-14]. These factors can lead to the formation of three types of *B*-cation ordering in DP structure, namely ideal rock-salt ordering, partial rock-salt ordering with local disorder, and complete disorder [15, 16]. Only recently, has the influence of the radius contrast between Mn and *B′* (*B′*= Zr, Hf, and Ti) been established on the structural ordering of $La_2MnB'O_6$ [17].

From a structural point of view, it is well known that the $A_2BB'O_6$ formula can be represented in the form of an alternating octahedra BO_6 and $B'O_6$ in a three-dimensional system (cations in *B*-sites

are connected in a pseudo-face-centered cube), while the vacant spaces between these octahedra are filled by *A* cations, 12-coordinatied as cuboctahedra [18].

It should be noted that DPs are not only characterized by their crystal structure transitions and, for example, magnetic transitions due to the above given aspects (ordering phenomena), which are considered as internal effects, but also due to external effects both physical (e.g. pressure and temperature) and chemical (e.g. substitution in the *A* and *B* sites) [19-22]. For instance, $SrCaCoTeO_6$ and $SrCaNiTeO_6$ show the following phase-transition sequence with increasing temperature:

$$P2_1/n(a^-a^-a^+) \rightarrow I2/m(a^-a^-a^0) \rightarrow I4/m(a^0a^0c^-) \rightarrow Fm\bar{3}m(a^0a^0a^0).$$

As an example, Mn_2MnTeO_6 experiences a magnetic phase transition from antiferromagnetic (AFM) to a complex magnetic structure with ordered magnetic moments at the *A* and *B* sites under high pressure [23, 24].

Here we report on the synthesis, crystal structure evolution and spectroscopic properties as a function of iron content in the new perovskite-type solid solution $Sr_2(Fe_{1-x}Ni_x)TeO_6$ (*x = 0, 0.25, 0.5, 0.75* and *1*), where the existing structure data for the end-members (*x = 0* and *1*) are used as isotypes for the refinement of the structures of the intermediate members of the solid solution. Regarding the composition Sr_2FeTeO_6, Ortega et al. have proposed a monoclinic structure, with the space group *I*2/*m* [25]. In their work a cationic disorder of Fe^{3+} and Te^{6+} was observed, which generate tellurium deficient with vacancies in *B*-site of the structure. This vacancy is responsible of charge compensation of the Fe^{3+} cations. As it is reported for most of double perovskite oxides with formula A_2MTeO_6 with *A* = Sr, Ba and *M* = Ni, Mn, Co, Cu... are very similar: they have a M^{2+} cation and a Te^{6+} cation fully ordered on the two *B*-sites, and Type I magnetic order at low temperatures [26-29]. Therefore, Sr_2FeTeO_6 is considered as unusual double perovskite. Moreover, the cationic distribution with the observed vacancies in the *B*-site of Sr_2FeTeO_6 impact as well the magnetic behaviour of this material, where the most important interactions found are of antiferromagnetic nature, and the sample shows spin-glass-like behaviour at low temperature. On the other hand, further studies have been on the Sr_2NiTeO_6 oxide. Iwanaga et al. [30] reported a monoclinic structure, with the space group *I*2/*m* for this double perovskite material, and the refinement shows a full *B*-site order by the reason of the big difference of charge between Ni^{2+} and Te^{6+} [30]. Both field-cooled and zero-field cooled DC magnetic susceptibility revealed that Ni^{2+} cations in the Sr_2NiTeO_6 compound are antiferromagnetically ordered. The J_1/J_2 can predict the magnetic ordering in the double perovskites, where two types of *B*-cations are paramagnetic, leading to so called type-I AFM spin-arrangement consisting of layers of ferromagnetic chains antiferromagnetically coupled [20, 31]. Thus, the solid solution $Sr_2Fe_{1-x}Ni_xTeO_6$ could be considered an interesting playground to study the Fe^{3+}, Ni^{2+} and Te^{6+} cations disordered across the *B* sites of double perovskites. Accordingly, the crystal structures for all the oxides are studied at room temperature via powder X-ray diffraction, with the data analyzed through the Rietveld method. SEM investigations are used to probe the morphology of this series, UV/Vis diffuse reflectance spectroscopy (DR-UV–vis) is

utilized to study the optical properties. The degree of cation ordering and dynamic structural changes are studied through room-temperature Raman measurements. Further, Mössbauer spectroscopy has provided crucial information regarding the spin and valence states of the substituted iron. The hyperfine parameters are consistent with the presence of two distinct crystallographic sites occupied by iron and reveal the effect of the cation distribution on the octahedral distortion in the DPs. From the temperature-dependent DC magnetic susceptibility measurements, the effect of *B*-site cation disorder on the magnetic properties of the DP series was observed. TGA/DSC measurements were performed to investigate the thermal stability of synthesized DP series.

2. EXPERIMENTAL

2.1. Materials and Methods:

Materials and Synthesis: All polycrystalline samples of the double perovskite series $Sr_2(Fe_{1-x}Ni_x)TeO_6$ (*x = 0, 0.25, 0.5, 0.75,* and *1*) were synthesized via solid-state reaction at high temperature from stoichiometric amounts of $SrCO_3$ (Sigma-Aldrich 99.9 %), $NiCO_3$ (Sigma-Aldrich 99.9 %), $Fe(NO_3)_3.9H_2O$ (Sigma-Aldrich 99.9 %), and TeO_2 (Sigma-Aldrich 99.9 %). The respective quantities were mixed and ground together in an agate mortar with the addition of ~1 mL acetone as a grinding aid. The mixtures were calcined in air in alumina crucibles according to the following the heating regime: (i) 850 K for 12 h; (ii) 1073 K for 24 h; (iii) 1173 K for 24 h; (iv) 1273 K for 48 h and (v) 1300 K for 48 h with a heating rate of 275 K min^{-1} in each case. Further, to increase and promote the homogeneity of the reaction, the samples were re-ground after each heat-treatment step. Phase-pure final samples were obtained.

Characterization techniques: Powder X-ray diffraction was performed at room temperature using a PANalytical X'Pert Pro diffractometer with a Cu $K_{\alpha1,2}$ radiation source ($\lambda k_{\alpha1}$ = 154.05929(5) pm, $\lambda k_{\alpha2}$ = 154.4414(2) pm), in a Bragg-Brentano reflection geometry. The data were collected in a 2θ range of $15^o \leq 2\theta \leq 100^o$ with a 0.0167º step size for 30 s $step^{-1}$. Rietveld refinement of the structures was subsequently conducted using the FullProf (integrated in Winplotr) [32, 33] and the TOPAS® software packages. The structures are visualized using VESTA [34]. The empirical crystal structure stability for each material was predicted by calculating the Goldschmidt tolerance factor [35] for a double perovskite, $A_2BB'O_6$, futher details are given in electronic supporting information (ESI).

Raman spectroscopy measurements were performed at room temperature using a Horiba LabRAM Aramis spectrometer configured with a Synapse CCD detector and a confocal Olympus BX-41 microscope. A 785 nm laser was used operating at less than 20 mW. Spectra were recorded from 100 to 850 cm^{-1} with a spectral resolution of approximately 1.2 cm^{-1} using a grating of 1800 grooves/mm.

The morphology, grain-size distribution and homogeneity of the prepared powders were examined by scanning electron microscopy (SEM) with a JMS-6510 (JEOL) microscope equipped with an X-Flash 410-M detector (Bruker) for energy dispersive X-ray spectroscopy (EDX). To increase the

conductivity of the samples, they were placed first on conductive carbon tabs (fixed on an aluminum stub) and deposited with gold for 20 s using a JFC-1200 (JEOL) coater.

All Mössbauer spectra were measured at room temperature with a velocity range +/- 4 mm/s. The samples were loaded into acrylic sample disks with an area of 1.767 cm^2. γ-rays of 14.4 keV were supplied by the cascade decay of 0.925 Gbq ^{57}Co in a rhodium matrix source oscillated at a constant acceleration by a SeeCo W304 drive unit. The detector is a SeeCo 45431 Kr proportional counter operating with a bias voltage of 1.720 kV applied to the cathode. Absorbers were prepared from ground samples mixed with graphite powder to ensure a Mössbauer thickness t<1. All measurements were calibrated relative to α-Fe foil, with all spectral data fitted using the Recoil software package [36], using Lorentzian line shapes. Conservative estimates of the uncertainties associated with fitting each component were as follows: Centre Shift +/-0.02 mm s^{-1}; Quadrupole Splitting +/-0.02 mm s^{-1}; Linewidth +/- 0.02 mm s^{-1}; and Relative Area +/-2 %.

The optical properties of the materials were studied by diffuse reflectance UV/Vis spectroscopy (DR-UV/Vis) and analyzed using the RATD method. Further details are given in ESI.

Thermal stability of this series of DP were measured by thermo-gravimetric analysis (TGA) coupled with Differential Scanning Calorimetry (DSC) using TGA/DSC 3+ STARe System of Mettler Toledo. The samples were measured with a heating rate of 10 K/min and a continuous N_2 flow of 20 mL/min from 300 to 1273 K. The compounds amounts are 23.17(1) mg, 20.6(1) mg, 19.67(1) mg, 20.4(1) mg, and 20.8(1) mg for *x = 0, 0.25, 0.5, 0.75* and *1*, respectively, which were measured relative to an empty corundum reference crucible.

The magnetic susceptibility of the samples was evaluated using a Quantum Design MPMS3 SQUID Magnetometer. Zero-field cooled and field-cooled measurements were taken from 5 to 300 K in applied field of 79577.471546 A/m. The data were corrected for the gelatin capsule and the diamagnetic contributions from the elemental constituents.

3. RESULTS AND DISCUSSION

3.1. Crystal structures at room temperature

Determination and description of the crystal structure:

The XRD diagrams of the series $Sr_2(Fe_{1-x}Ni_x)TeO_6$ measured at room temperature are presented in **Figure 1**. The patterns show a fundamental similarity in peak sequences with those of other DP structures [25, 29]. On closer scrutiny, most of these reflections are split, confirming a deviation from the cubic aristotype phase characteristic for many DPs. The peak positions in the patterns demonstrate a subtle shift to higher 2θ angle with increasing nickel content, *x*.

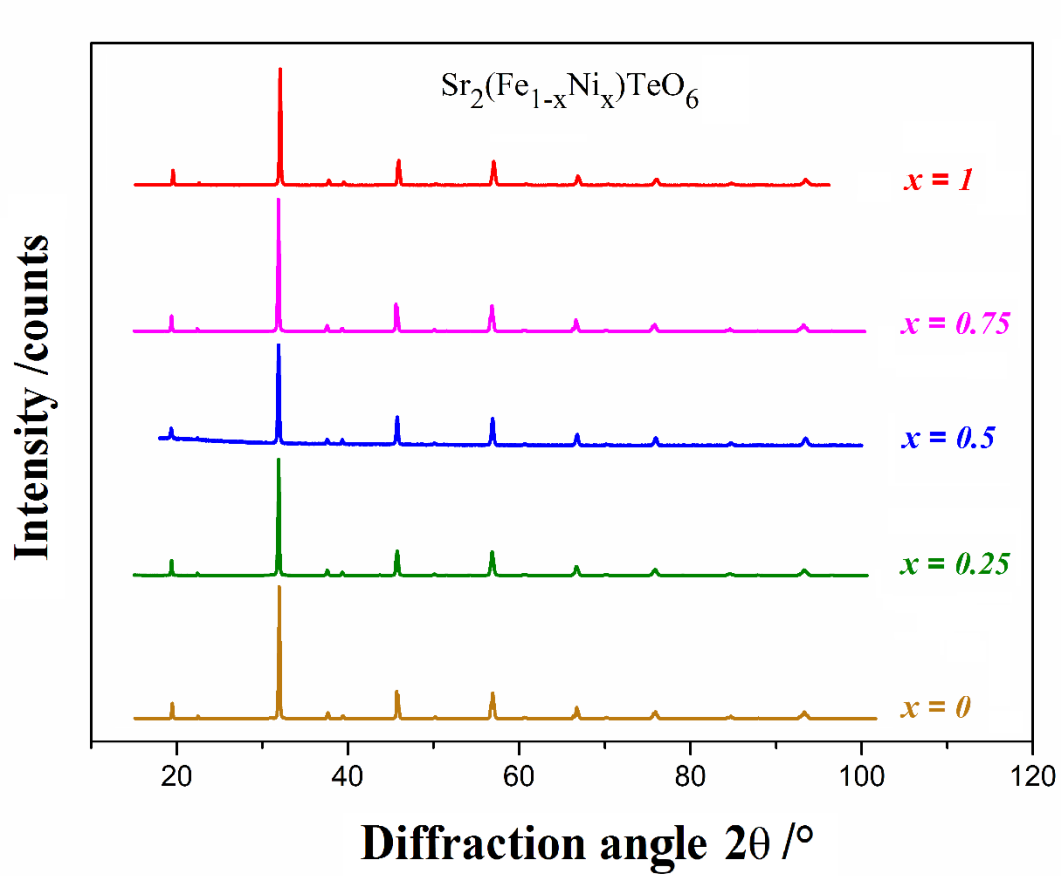

Figure 1: XRD patterns of DP $Sr_2(Fe_{1-x}Ni_x)TeO_6$ measured at room temperature.

In order, to initiate a structure refinement, the Rietveld method demands a structural model. Since the three intermediate compositions of this series $Sr_2(Fe_{0.75}Ni_{0.25})TeO_6$, $Sr_2(Fe_{0.50}Ni_{0.50})TeO_6$, and $Sr_2(Fe_{0.25}Ni_{0.75})TeO_6$ are isostructural with Sr_2FeTeO_6 and Sr_2NiTeO_6 according to the data in **Figure 1**, the monoclinic structures of the ferrate and nickelate (space group *I*2/*m*; corresponding with the tilt system ($a^-a^-c^0$) following Glazer's notation [37]) were initially adopted to describe the *x = 0.25*, *0.50* and *0.75* compositions. In this model, Sr, Fe/Ni and Te are respectively located at the 4*i* (*x*, 0, *z*), 2*d* (½, ½, 0) and 2*a* (0, 0, 0) sites, with two crystallographic distinct oxygen atoms, O1 4*i* (*x*, 0, *z*) and O2 8*j* (*x*, *y*, *z*)) present. The difference in charge between cations on the nominal *B*(Fe/Ni)^{2d} and *B'*(Te)^{2a} sites, is used to account for their assumed initial ordering. Since the results of Rietveld refinement were obtained based on X-ray data, it was very difficult to solve the site disorder, vacancies and the Ni-doping on the *B*-site. However, the followed Rietveld refinement strategy of these parameters (occupancies, vacancies and site disorder) were used. First, a free refinement of Fe occupancy on the *2d* site was allowed, and then the Fe/Te occupancies on the *2a* site get another parameter which is $Te_{occ.} = 1 - Fe_{occ}$. As a result, a partial disorder occurs when the atoms of Fe set together with Te (a cationic distribution of Fe from *2d* site to *2a* site is happened), with the appearance of vacancies in *2d* site, and this to make charge compensation of the Fe^{3+} cations in the system. This strategy gave similar results to the one reported by Ortega et al. [25]. Concerning the other compositions with Ni-doping, the same method of refinement

was used with keeping the Ni atoms only on the *2d* site. As the formation of the vacancies are related to the location of Fe with Te, it is normal that the number of vacancies is decreasing as Fe quantity deceases, as well as there is a decreasing in the degree of disorder in the systems, in which this series of double perovskites goes from partial disorder with vacancies at $x = 0$ to full site order for $x = 1$. It is worth to mention that the *B*-site occupancies are subject to significant uncertainty, and that the displacement parameters for all the atoms (Sr^{2+}, Fe^{3+}, Ni^{2+}, Te^{6+} and O^{2-}) were fixed during the refinement. **Tables 2** and **3** summarize the structural details of the DP series following refinement. The resolved fractional occupancies of the various *B* atoms (Fe, Ni, and Te) across the 2*d* and 2*a* sites are represented in **Table 3**. The obtained fractions were checked and verified based on the calculated bond valence sums (BVS) of Fe/Ni and Te, which shows that the refined models were consistent with the formal valences of these elements (Sr^{2+}, Fe^{3+}, Ni^{2+}, Te^{6+} and O^{2-}). The final Rietveld plot for the $x = 0.50$ is given in **Figure 2** showing very good agreement between the observed and calculated XRD patterns at room temperature (profiles for the other compositions are collected in **Figure S1** in the supplementary information).

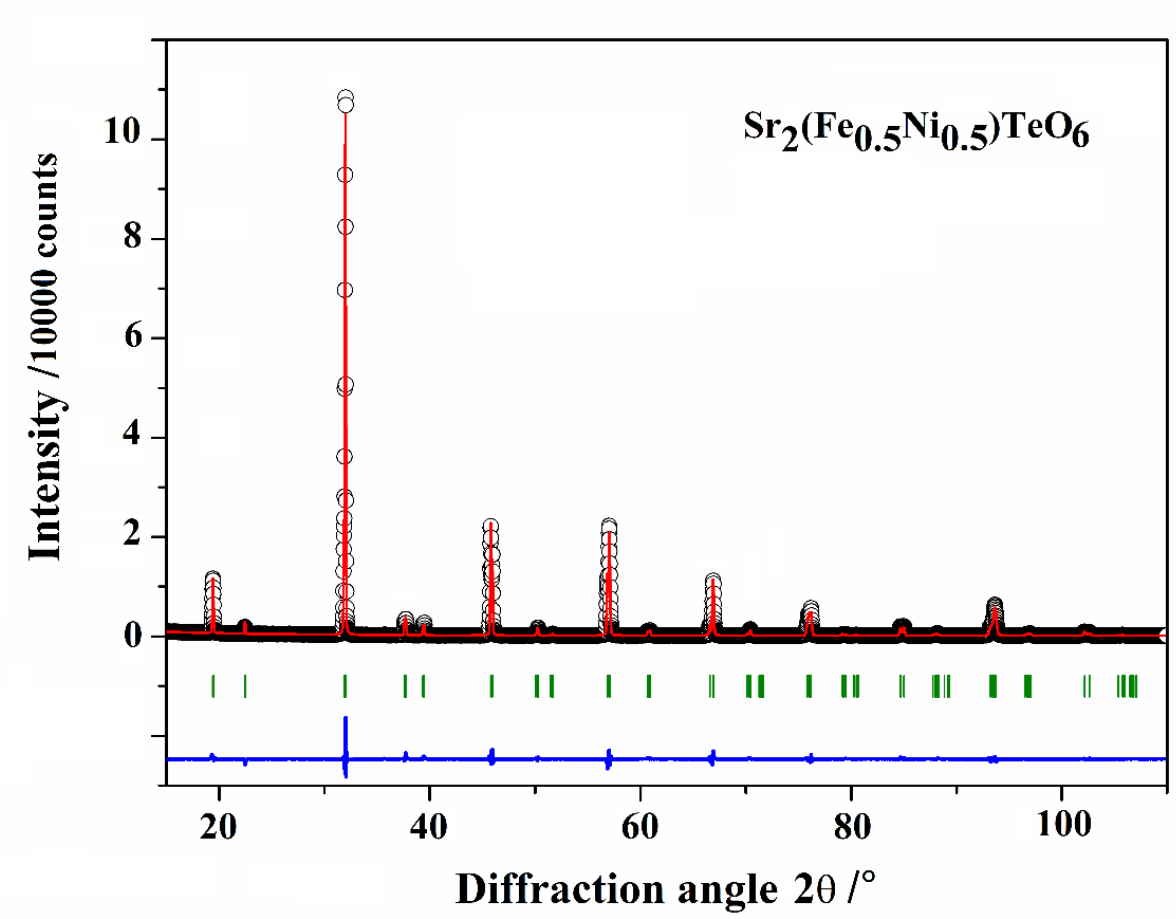

Figure 2: Rietveld plot for the composition $Sr_2[Fe_{0.41}Ni_{0.5}\square_{0.09}]^{2d}[Te_{0.94}Fe_{0.06}]^{2a}O_6$ (□ : vacancy). The experimental pattern is indicated by black circles, the calculated intensities by the solid red line and the difference profile by the blue solid line. Vertical green markers indicate the respective DP Bragg reflections.

The Goldschmidt tolerance factors (*t*), were calculated to be less than 1 for all the compositions. This suggests that the room-temperature structures of the compounds should be distorted from the cubic model. Moreover, the decrease of the *t* values reveals the expected increased distortion as Fe is substituted by Ni. **Table 1** lists the calculated tolerance factors for the solid solution.

Table 1: Tolerance factor of $Sr_2(Fe_{1-x}Ni_x)TeO_6$ calculated using the ionic radii given by Shannon [1] (see electronic supplementary information references)

Composition	Tolerance factor
x = 0.00	0.998(2)
x = 0.25	0.994(1)
x = 0.50	0.993(2)
x = 0.75	0.992(2)
x = 1.00	0.991(2)

The evolution of the lattice parameters as a function of both the calculated tolerance factor and the nickel content, *x* is represented in **Figure 3**. Given that the tolerance factors vary in line with the ionic radii of the component Fe, Ni, and Te (see **Table 2**), the evolution of the cell parameters shows a decrease with increasing nickel, *x* (tolerance factor, *t*), with the exception of the *a* parameter which displays the opposite behavior. Nevertheless, there is a decrease in overall cell volume as Ni replaces Fe. This cell volume reduction with increased Ni content represents a second indication of the presence of HS Fe^{2+} within the system. From the observed behavior of the cell parameters with *x* and *t*, it is apparent that Vegard's law is upheld in this DP series [38].

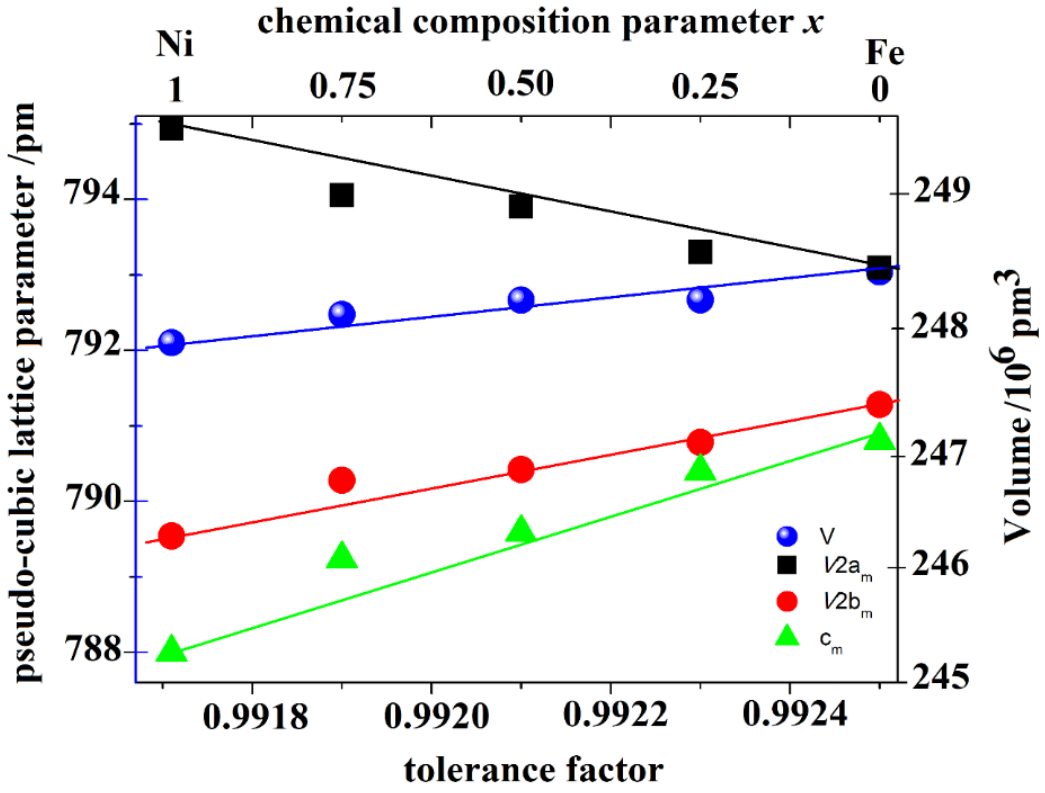

Figure 3. Metric parameters as a function of tolerance factor (bottom axis) and Ni stoichiometry, *x* (top *x* axis) for the DP series, $Sr_2(Fe_{1-x}Ni_x)TeO_6$ (*x = 0, 0.25, 0.5, 0.75* and *1*). The values of a and b have been scaled by a factor of √2 for clarity.

Table 2: Crystallographic data for $Sr_2(Fe_{1-x}Ni_x)TeO_6$ (*x = 0, 0.25, 0.5, 0.75*and *1*)

Compositions	x = 0	x = 0.25	x = 0.5	x = 0.75	x = 1
Space group	*I2/m*	*I2/m*	*I2/m*	*I2/m*	*I2/m*
a /pm	561.86(1)	561.45(2)	561.21(1)	561.09(6)	559.96(1)
b /pm	559.25 (1)	559.47(2)	559.81(1)	559.89(7)	559.92(1)
c /pm	788.94(1)	789.78(2)	790.09(1)	790.24(8)	790.98(1)
β /°	89.98(1)	89.988(1)	90.006(1)	90.03(4)	90.056(2)
V /10^6pm^3	248.19(2)	248.348(1)	248.040(2)	248.155(2)	246.97(2)
Z	2	2	2	2	2
R_p	10.02	10.5	8.32	6.53	7.07
R_{wp}	14.1	14.4	10.4	8.76	9.18
R_{exp}	8.70	5.72	3.57	2.70	6.74
R_B	5.06	9.58	2.78	1.99	4.71
R_F	3.77	9.35	3.06	1.88	7.17
χ^2	2.62	6.30	8.44	10.5	1.85

The atomic positions, isotropic displacement parameters and site occupancies are shown in **Table 3**. Selected bond distances with internal and external angles are listed in **Table 4**. The bond lengths are in good agreement with distances derived from sums of Shannon's cationic radii with O^{2-} in 6-coordinate environment. The structure models for the *2d* (Fe/Ni/Te) and *2a* (Fe/Ni/Te) sites are therefore consistent with BO_6 octahedra. Moreover, bond lengths closely resemble those reported for

the "parent" DP compounds, Sr_2FeTeO_6 and Sr_2NiTeO_6 [25, 29]. Consequently, from the data obtained, it is evident that the octahedra centered at the *2a* site are smaller than those constructed around the *2d* site, and that both of them are slightly distorted (as seen in **Figure S2** in supplementary information). In three dimension, the two different octahedral types are connected through O(1) along the c-axis, through O(2) in the *ab* plane.

Table 3: Atomic positions, thermal displacement and occupation parameters for $Sr_2(Fe_{1-x}Ni_x)TeO_6$ (*x = 0, 0.25, 0.50, 0.75* and *1*) obtained from the Rietveld refinements against XRD data collected at room temperature. All structures are in monoclinic space group, *I2/m*. (□) : vacancy.

Atom	Wyckoff site	x	y	z	$B/10^6pm^2$	Fractional occupancy
Sr_2FeTeO_6, (*I*2/*m*)						
Sr	*4i*	0.4981(2)	0	0.7556(2)	0.79(2)	1
Fe1/(□)	*2d*	0.5	0.5	0	1.03(2)	0.86(3)/0.14(3)
Te/Fe2	*2a*	0	0	0	0.71(2)	0.89(3)/0.11(3)
O1	*4i*	0.0195(2)	0	0.7550 (2)	1.57(2)	1
O2	*8j*	0.268(2)	0.227(2)	0.9157 (2)	2.04(2)	1
$Sr_2(Fe_{0.75}Ni_{0.25})TeO_6$ (*I*2/*m*)						
Sr	*4i*	0.5118(3)	0	0.7496 (3)	2.34(2)	1
Fe1/Ni/(□)	*2d*	0.5	0.5	0	0.52(2)	0.64(3)/0.25(1)/0.11(3)
Te/Fe2	*2a*	0	0	0	2.62(3)	0.90(3)/0.10(3)
O1	*4i*	0.033(3)	0	0.7625(3)	0.11(3)	1
O2	*8j*	0.268(3)	0.248(3)	0.9918(3)	0.11(3)	1
$Sr_2(Fe_{0.50}Ni_{0.50})TeO_6$ (*I*2/*m*)						
Sr	*4i*	0.5023(3)	0	0.7503(3)	0.64(3)	1
Fe1/Ni/(□)	*2d*	0.5	0.5	0	0.46(3)	0.41(3)/0.50(1)/0.09(3)
Te/Fe2	*2a*	0	0	0	0.54(2)	0.94(3)/0.06(4)
O1	*4i*	0.043(3)	0	0.7551(3)	0.10(3)	1
O2	*8j*	0.2434(2)	0.2405(1)	0.9986(3)	0.10(3)	1
$Sr_2(Fe_{0.25}Ni_{0.75})TeO_6$ (*I*2/*m*)						
Sr	*4i*	0.5043(2)	0	0.7503(2)	0.72(2)	1
Fe1/Ni/(□)	*2d*	0.5	0.5	0	0.19(3)	0.16(3)/0.75(1)/0.09(3)
Te/Fe2	*2a*	0	0	0	0.93(2)	0.91(3)/0.09(3)
O1	*4i*	0.042(2)	0	0.758(2)	0.18(3)	1
O2	*8j*	0.2367(2)	0.2431(1)	0.9969(2)	0.18(3)	1
Sr_2NiTeO_6 (*I*2/*m*)						
Sr	*4i*	0.502(2)	0	0.7514(3)	0.64(2)	1
Ni	*2d*	0.5	0.5	0	0.31(3)	1
Te	*2a*	0	0	0	0.78(3)	1
O1	*4i*	0.057(3)	0	0.738(2)	0.24(2)	1
O2	*8j*	0.210(2)	0.250(2)	0.997(2)	0.24(3)	1

Table 4: Selected room-temperature inter-atomic distances and angles for $Sr_2(Fe_{1-x}Ni_x)TeO_6$ (*x = 0, 0.25, 0.50, 0.75* and *1*).

Compositions	*x=0*	*x=0.25*	*x=0.5*	x=0.75	*x=1*
Octahedra site: (*2d*)					
Fe/Ni – O1	193(2)	202(2)	204(2)	207(2)	209(2)
Fe2/Te – O2	191.1(2)	195(2)	196(2)	202(2)	201(2)

Average distance /pm	192(2)	198.5(2)	200(2)	204.5(2)	205(2)
Predicted distance /pm	206(2)	206(2)	206(2)	206(2)	206(2)
Octahedra site: (*2a*)					
Fe/Ni/Te – O1	191(2)	192(2)	193(2)	192(2)	192.6(2)
Fe/Ni/Te – O2	195(2)	199(2)	196(2)	195.4(2)	191.6(2)
Average distance /pm	195.7(2)	195(2)	194(2)	193(2)	192.1(2)
Predicted distance /pm	190(2)	190(2)	190(2)	190(2)	190(2)
Internal angles/ °					
2d site: O1 – Fe/Ni/Te – O2	90.0(2)	92.90(1)	92.30(2)	92.90(1)	90.06(5)
2d site: O2 – Fe/Ni/Te – O2	91.80(2)	93(2)	92.20(2)	93.30(1)	91.60(2)
2a site: O1 – Fe/Ni/Te – O2	90.90(1)	93(1)	92.10(2)	93.40(2)	90.0(1)
2a site: O2 – fe/Ni/Te – O2	93.0(1)	92(2)	91.50(1)	90.40(2)	90.1(2)
External angles/ °					
Fe/Ni – O1 – Te	167.2(3)	175.40(2)	163.50(3)	165.40(3)	164.5(2)
Fe/Ni – O2 - Te	172.0(2)	158(2)	172.50(1)	163.10(2)	169.0(3)

3.2. Morphology of $Sr_2(Fe_{1-x}Ni_x)TeO_6$ series

SEM and EDX experiments were performed to examine the morphology of this series of materials and to gain further insight into the chemical composition, respectively. As revealed in **Figure S3** (see Supplementary information), the microstructures of all the samples are rather similar. Each is composed of large particles, with a relatively narrow particle size distribution. These observations are unsurprising considering the high temperatures used throughout the calcination process and the likely sintering that would result. Similar morphology and size distribution were observed previously for Sr_2FeTeO_6 and Sr_2NiTeO_6 [25, 39]. **Figure S3** collates the energy-dispersive X-ray (EDX) spectra taken for the samples. The EDX data showed that the samples contained only Sr, Fe, Ni, Te, and O as expected with additional carbon from the substrate detected. The results show that $Sr_2(Fe_{0.50}Ni_{0.50})TeO_6$ consists of 64(3) at% O, 4(1) at% Fe, 3(1) at% Ni, 9(1) at% Te and 20(1) at% Sr (EDX for the other compositions are collected in **Table S1** in the supplementary information). The transition metals and Te ratios were in reasonable agreement with the refined (and nominal) values and follow the expected trend as Ni replaced Fe in the DP structure.

3.3. Vibrational properties using Raman spectroscopy

To advance the understanding of the structural bonding behavior as well as to obtain more information about the bonding type of atoms in this structure, Raman spectroscopy was performed at room temperature. A full group theory analysis was used to interpret the spectra [40]. If this DP series crystallizes in a body-centered monoclinic space group (*I*2/*m*; point group C_{2h}), the appropriate irreducible representation can be defined as follows:

$$\Gamma\,(I2/m) = 7A_g\,(R) + 5B_g\,(R) + 7A_u\,(IR) + 11B_u\,(IR) + A_u\,(ac) + 2B_u\,(ac)$$

where, R represents Raman-active modes, IR represents infrared-active modes and ac refers to acoustic modes. From **Table 5**, the expected bands that should be observed comprise 13 Raman-active modes (7Ag + 5Bg), 18 infrared-active modes (7Au + 11Bu) and 3 acoustic modes (Au + 2Bu). From **Figure 4** it is evident that the Lorentzian fit from the group theory analysis is in excellent agreement with the experimental data. A total of 13 Raman modes are obtained for each of the samples (see **Figure S4** in the supplementary information for compositions *0.25, 0.50, 0.75* and *1*).

Table 5 : Analysis of factor group of double-perovskite series $Sr_2(Fe_{1-x}Ni_x)TeO_6$ at room temperature

Symmetry	**Atom**	**Site**	**A_g**	**A_u**	**B_g**	**B_u**	**Modes**
*I*2/*m*	Te	2a		1		2	$1A_u + 2B_u$
	Fe/Ni	2d		1		2	$1A_u + 2B_u$
	Sr	4i	2	1	1	2	$2A_g + A_u + B_g + 2B_u$
	O (1)	4i	2	1	1	2	$2A_g + A_u + B_g + 2B_u$
	O (2)	8j	3	3	3	3	$3A_g + 3A_u + 3B_g + 3B_u$
	$\boldsymbol{T}_{Total} = 14A + 16B = 30$, $\boldsymbol{T}$acoustic $= A_u + 2B_u$						
	$T_{Raman} = 7A_g + 5B_g$, $\boldsymbol{T}_{Infrared} = 7A_u + 11B_u$						

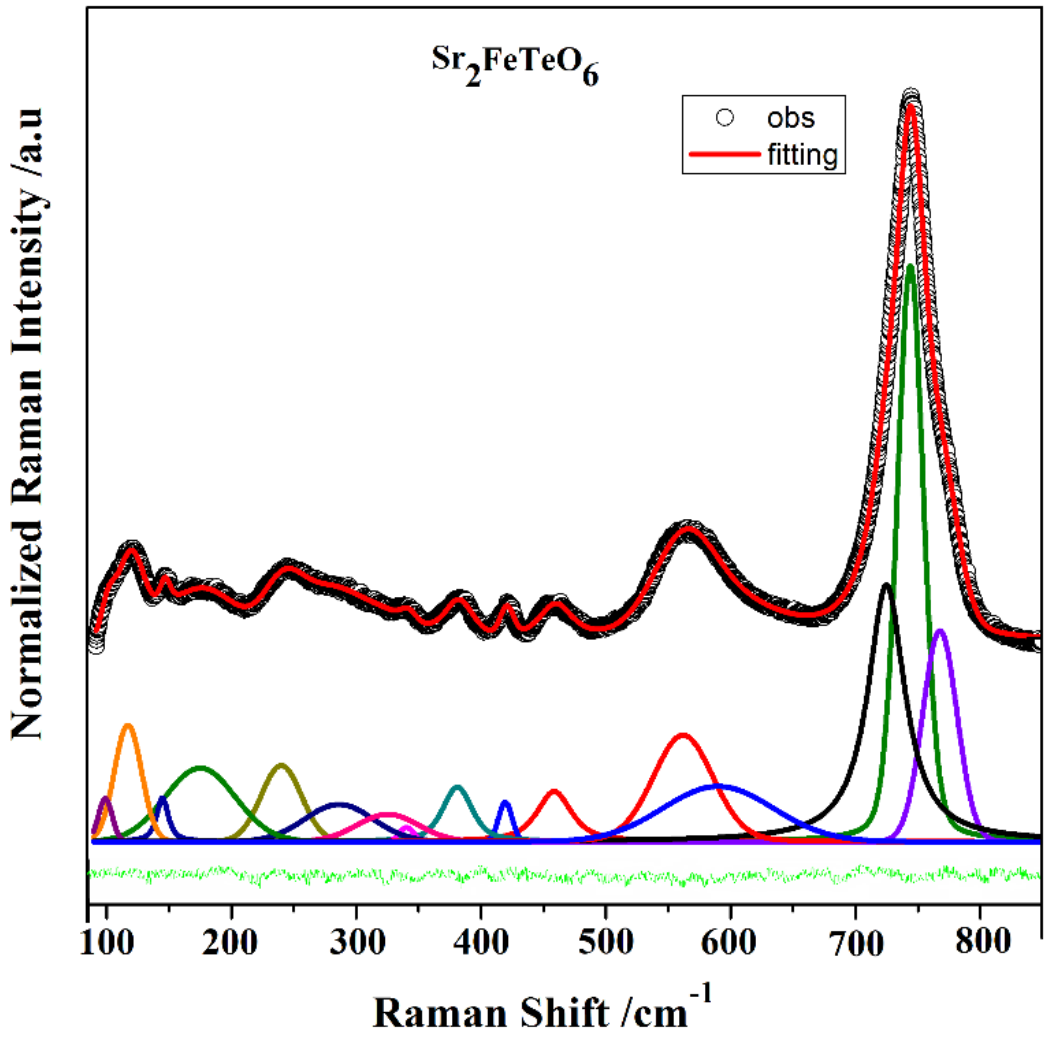

Figure 4. Room-temperature Raman data (black) for Sr_2FeTeO_6 together with the fitted Lorentzian peaks, the sum of the fitted peaks (red) and the difference curve (green).

The Raman spectra for the DP structures can be divided into three sections according to the observed modes (**Figure 5a**). The first section exist at wavenumbers <350 cm^{-1}, corresponding to translations of Sr^{2+} cations and translations and rotations of $(Fe/Ni/Te)O_6$ octahedra. The second set of bands (*υ5* and *υ2*), which are present between 350-500 cm^{-1}, related to the bonding of oxide with atoms in B-sites, O – (Fe/Ni/Te) – O. Finally, the stretching modes (*υ1*), which correspond to the (Fe/Ni/Te) – O bonds are located at frequencies >550 cm^{-1} [18].

As shown in **Figure 5a**, the Raman spectra of this series are dominated by bands at high wavenumbers, which correspond to the octahedral bonds of *2a* site (Fe/Ni/Te – O). These can be identified with the internal modes (*υ1*) [21] and are located at 745(1) cm^{-1}, 752(1) cm^{-1}, 755(1) cm^{-1}, 757(1) cm^{-1} and 762(1) cm^{-1} for *x = 0, 0.25, 0.5, 075* and *1*, respectively. **Figure 5b** shows the significant shift of these Raman modes -located at *ca.* 750 cm^{-1}- as the nickel content increase. These shifts indicate the ongoing distortion of the octahedra with *x*. Since these modes correspond to the Te/Fe/Ni – O (*2a* site) bonds, their expansion is explained by an increase in their bonding energy [41]. From the XRD results presented in **Table 4**, it is apparent that the Te/Fe/Ni (*2a* site) – O distances diminish as nickel replaces iron (i.e. with increasing *x*), which is consistent with an increase in the bond strength (energy). Accordingly, the frequency of the modes increases. The observed splitting of the Raman peaks at low frequencies attests to the crystallization of the structure in a monoclinic system. These regions of modes (located around 140 cm^{-1} and 450 cm^{-1}) are known to be affected by the monoclinic distortion in double perovskite, either by changing the chemical composition and/or temperature. The splitting of Raman modes is a consequence of octahedral distortion, which is explained by a degeneration of the vibrational energy levels and then the appearance of Raman modes split [42, 43]. The observed broad peaks located between 550 cm^{-1} and 650 cm^{-1}, which are fitted into 2 or 3 Lorentzian peaks, is due to the cationic disordering in *B*-sites [44]. The splitting and the broadening of the peaks are increasing with Fe substitution. The tolerance factor values are in good accord with what is observed in Raman modes, which show a decrease with increasing Ni, which means that the structure of composition Sr_2NiTeO_6 is more distorted than the structure of the composition Sr_2FeTeO_6.

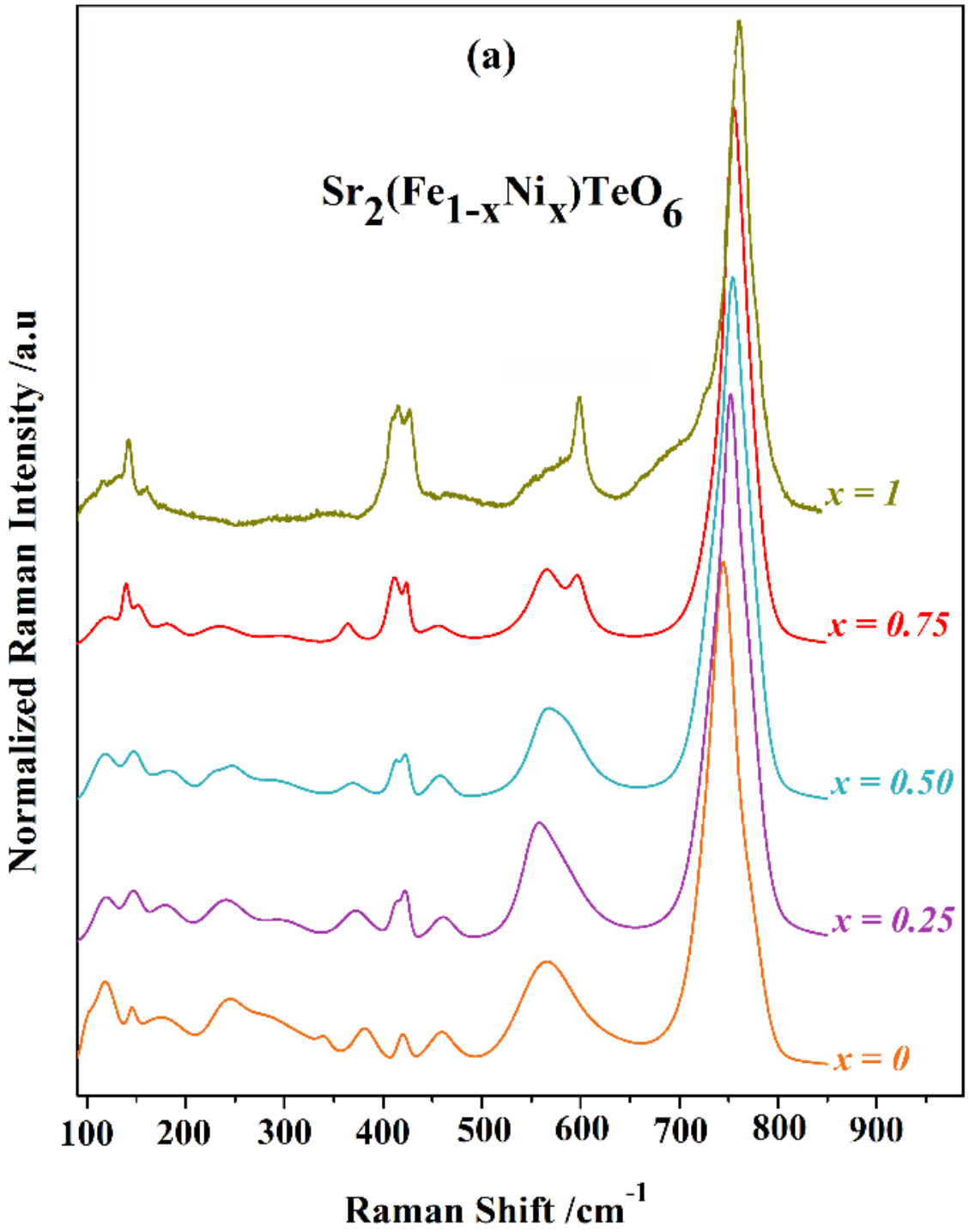
(a)
Sr2(Fe1-xNix)TeO6
Normalized Raman Intensity /a.u
x = 1
x = 0.75
x = 0.50
x = 0.25
x = 0
100
200
300
400
500
600
700
800
900
Raman Shift /cm-1

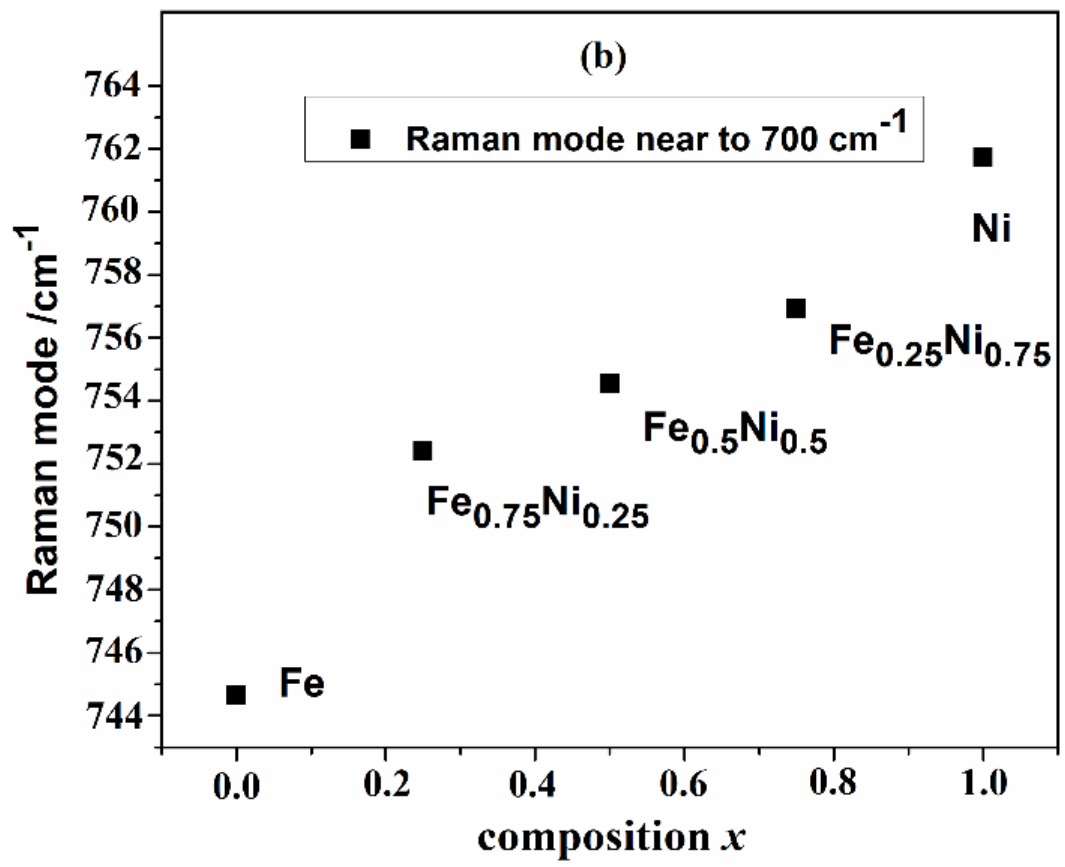

Figure 5. (a) Room-temperature Raman spectra of $Sr_2(Fe_{1-x}Ni_x)TeO_6$. **(b)** The evolution of Raman mode at approximately 750 cm^{-1} as a function of composition, *x*.

3.4. Optical properties

The UV/Vis spectra of the samples are investigated with the aim of probing their optical properties. **Figure 6** presents the UV/Vis diffuse reflectance spectra and the resulting Kubelka-Munk plots respectively, for the $Sr_2(Fe_{1-x}Ni_x)TeO_6$ samples [5] (see electronic suplementary references). As might be expected, the as-measured spectra suggest very similar electronic transitions in each sample with an approximate progression of the absorption edge to lower wavelength as *x* increases. The slight exception to this trend is the *x=1* sample, Sr_2NiTeO_6, which exhibits more pronounced electronic transitions and a disproportionately large increase in edge wavelength ; the nickelate evidently reflects much more strongly than the ferrates. For Sr_2NiTeO_6, the bands can be assigned to the respective d-d transitions located at *c.a.* 480(2), 520(2), and 740(2) nm. The first and second bands relate to the $^3A_{2g} \rightarrow {}^1T_{2g}$ and $^1E(D)$ transitions, whereas the third band is the spin-allowed transition $^3A_{2g} \rightarrow {}^3T_{1g}(P)$. The low reflectivity observed in the ferrate (*x<1*) spectra, signifies the higher absorption for the composition containing Fe. This is consistent with the dark brown colour of the iron-containing samples, while the nickel-containing sample has a light green colouration.

(a)

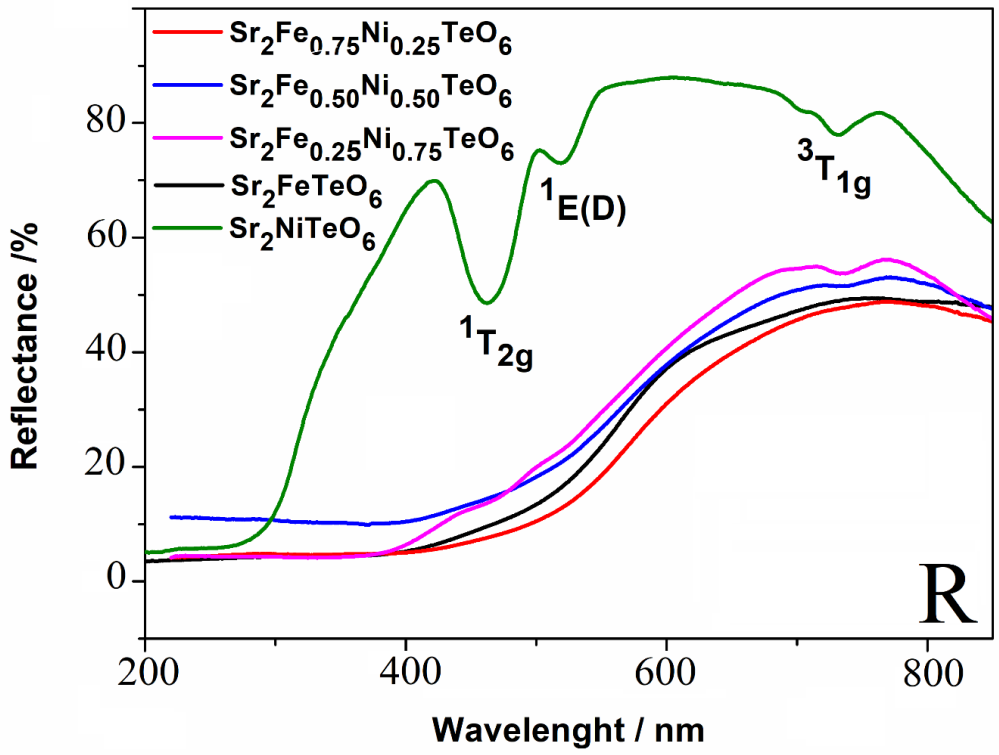
Sr2Fe0.75Ni0.25TeO6
Sr2Fe0.50Ni0.50TeO6
Sr2Fe0.25Ni0.75TeO6
Sr2FeTeO6
Sr2NiTeO6
1T2g
1E(D)
3T1g
R
Reflectance /%
Wavelenght / nm
0
20
40
60
80
200
400
600
800

(b)

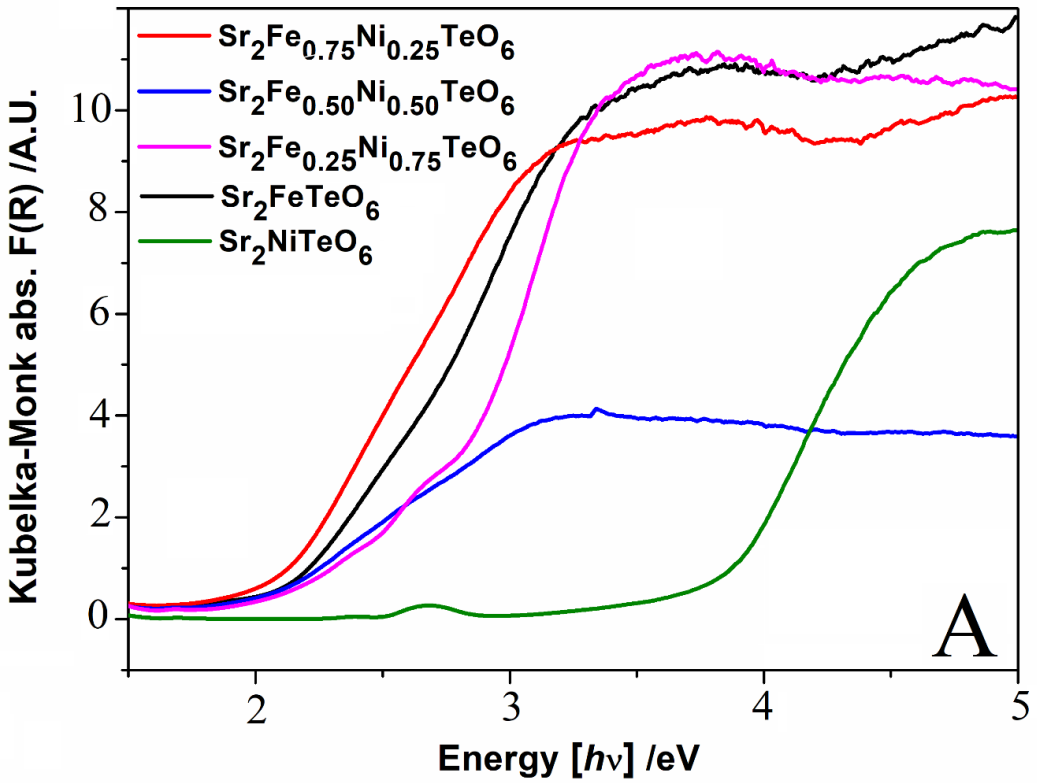
Sr2Fe0.75Ni0.25TeO6
Sr2Fe0.50Ni0.50TeO6
Sr2Fe0.25Ni0.75TeO6
Sr2FeTeO6
Sr2NiTeO6
A
Kubelka-Monk abs. F(R) /A.U.
Energy [hν] /eV
0
2
4
6
8
10
2
3
4
5

Figure 6. **(a)** Reflectance (***R***) versus λ (top) with **(b)** Kubelka-Munk function $F(R) \approx \boldsymbol{A}(\lambda)$ spectra versus $h\upsilon$ without considering electronic transitions (bottom).

Two methods were used to fit the DR-UV-Vis data in order to extract the band gap energies. First the Tauc method [53, 54], was applied, considering n = 2 or ½ for indirect and direct band gap transitions respectively as per the Kubelka-Munk function (equation 3). Secondly, DASF methods (Derivation of absorption spectrum fitting [5, 47 and 48]) (for refence 5, see electronic supplementary information references) were applied (equation 5). **Figure 7** exhibits the results obtained from each respective method of analysis for composition $x = 0$. The combination of methods indicates a direct band gap for all the compositions (see **Figure S5** in supplementary information).

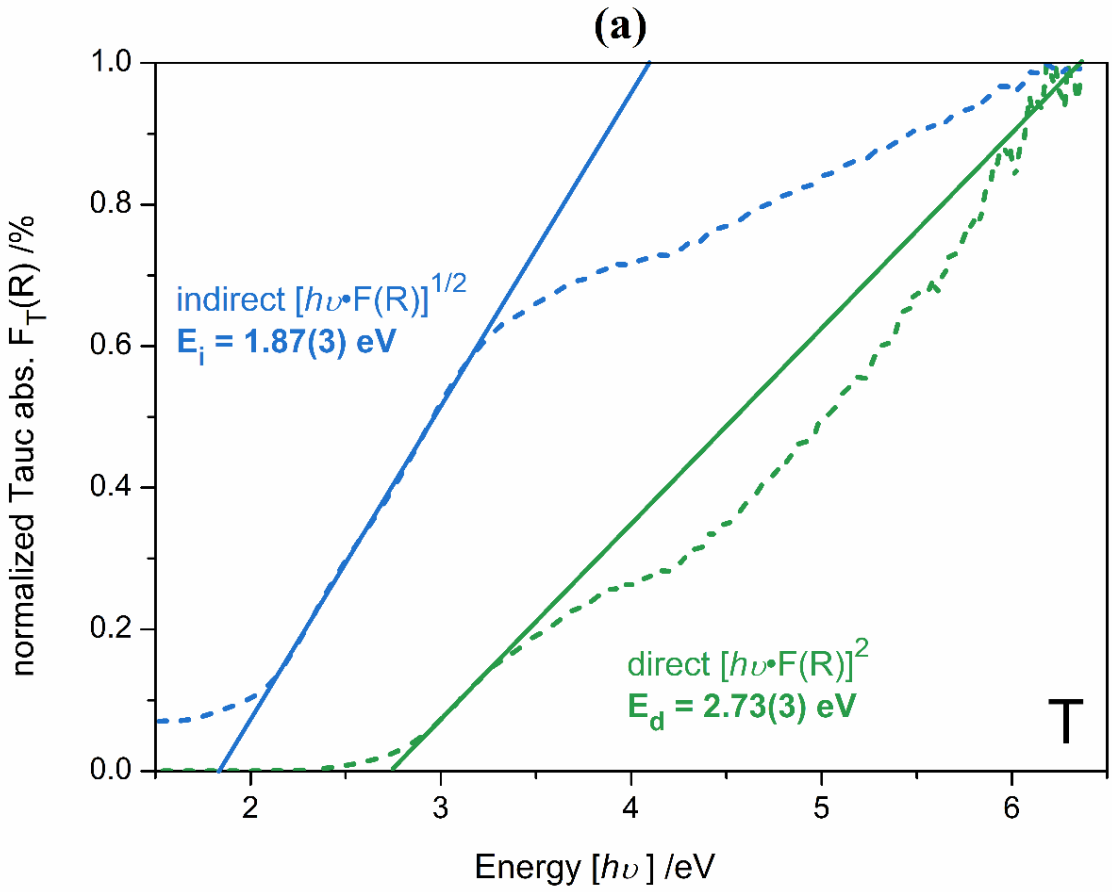

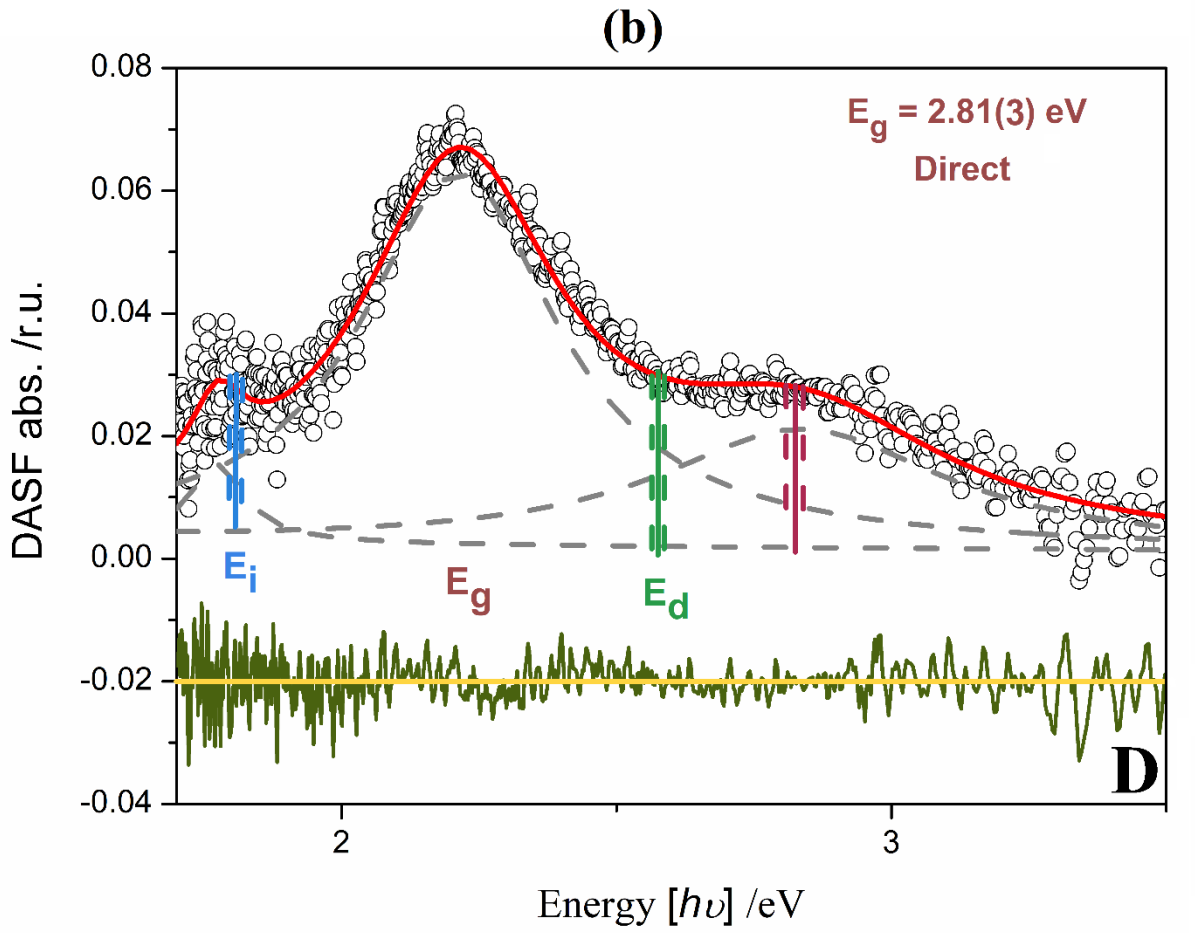

Figure 7. (a). Tauc plots for direct $(h\upsilon * F(R))^2$ and indirect $(h\upsilon * F(R))^{1/2}$ (top) with **(b).** DASF plots (bottom) for Sr_2FeTeO_6.

Table 6: Experimental values of the absolute band gap energy $\boldsymbol{E_g}$ obtained from different graphic methods for DP $Sr_2(Fe_{1-x}\ Ni_x)TeO_6$.

Method	Band gap energy [eV]				
	x = 0	*x = 0.25*	*x = 0.5*	*x = 0.75*	*x = 1*
Indirect $(h\upsilon * F(R))^{1/2}$	1.87(3)	1.84(3)	1.85(3)	2.38(3)	3.60(3)
Direct $(h\upsilon * F(R))^2$	2.73(3)	2.56(3)	2.57(3)	2.93(3)	4.10(3)
$\boldsymbol{E_g}$	***2.81(3)***	***2.84(3)***	***2.93(3)***	***3.23(3)***	***3.97(3)***

The choice of the transition type either direct or indirect was based on the comparison of the difference value found between $\boldsymbol{E_g}$ and the values of E_d (direct) and E_i (indirect). The smaller the value of this difference, the more it helps in estimating the transition type that the material has [9] (see electronic supplementary information references). For instance, the composition Sr_2FeTeO_6 has a value of $\boldsymbol{E_g}$ = 2.81(3) eV near to the E_d = 2.73(3) eV, which suggests a direct transition for this material. The same with the composition Sr_2NiTeO_6, the $\boldsymbol{E_g}$ value 3.97(3) eV is very close to the E_d value 4.10(3) eV, and that confirms a direct transition for this compound. Regarding the compounds *x = 0.25, 0.50* and *0.75*, they showed a direct transition as well as *x = 0* and *1*.

The results in **Table 6** indicate that the value of E_g increases with higher nickel content, *x*. This continues to increase at *x=1*, when all the iron is replaced by nickel. The size of the bandgap is influenced by the ionic radius of *B*, which also affects the transition distance of the electrons in valence band; as the ionic radius decreases the transition distance increases, as does the band gap [49, 50]. Similar observations regarding the effect of the ionic radius on the bandgap energy trend were reported by F. I. H. Alias et al. [51] for the series $Sr_2Ni_{1-x}Zn_xTeO_6$.

3.5. ^{57}Fe Mössbauer spectroscopy

Given the questions raised by the structural trends and the band-gap sequences in the series, room temperature ^{57}Fe Mössbauer spectroscopy measurements were performed on each of the ferrate DP samples, $Sr_2(Fe_{1-x}Ni_x)TeO_6$ (*x = 0, 0.25, 0.50* and *0.75*) to verify the electronic configurations and the crystallographic environments of the Fe ions. **Figure S6** displays the paramagnetic spectra of the samples where three doublets were fitted to the spectra for the compositions which contain a high percentage of Fe (*x = 0, 0.25* and *0.50*). However, the Mössbauer spectrum for the sample with composition *x = 0.75* ($Sr_2Fe_{0.25}Ni_{0.75}TeO_6$) exhibits two strong doublets. The best fits to the spectra were made using a superposition of quadrupole doublets in three paramagnetic doublets, and as is apparent from the fit parameters, χ^2 (0.7003, 0.660413, 0.759798 and 0.63213 for *x = 0, 0.25, 0.50* and *0.75*, respectively), sufficiently robust fits were indeed achieved. **Table 7** lists the hyperfine parameters obtained from the fits to the Mössbauer data.

Table 7: Hyperfine parameters of the DP ferrates $Sr_2(Fe_{1-x}Ni_x)TeO_6$ (*x = 0, 0.25, 0.5* and *0.75*) at ambient temperature (CS: centre shift, QS: quadrupole splitting, Γ: the line width given as the half-width, half-maximum (FWHM))

Compositions		CS / mm s^{-1}	QS / mm s^{-1}	Γ / mm s^{-1}	Relative Area /%
x = 0 Sr_2FeTeO_6	Paramagnetic-doublet	0.456(1)	2.062(1)	0.315(1)	14.0(1)
	Iron – *2a* Site	0.441(1)	1.225(1)	0.187(1)	42.4(1)
	Iron – *2d* Site	0.449(1)	0.234(1)	0.302(1)	44.0(1)
x = 0.25 $Sr_2(Fe_{0.75}Ni_{0.25})TeO_6$	Paramagnetic-doublet	0.462(1)	2.314(1)	0.127(1)	4.4(1)
	Iron - *2a* Site	0.443(1)	1.226(1)	0.200(1)	57.7(1)
	Iron - *2d* Site	0.452(1)	0.252(1)	0.208(1)	38.1(1)
x = 0.5 $Sr_2(Fe_{0.50}Ni_{0.50})TeO_6$	Paramagnetic-doublet	0.273(1)	2.461(1)	0.101(1)	4.0(1)
	Iron - *2a* Site	0.453(1)	1.253(1)	0.189(1)	54.1(1)
	Iron - *2d* Site	0.488(1)	0.220(1)	0.240(1)	42.1(1)
	Iron - *2a* Site	0.463(1)	1.294(1)	0.172(1)	35.2(1)

x = 0.75 ($Sr_2Fe_{0.25}Ni_{0.75}TeO_6$)	Iron - *2d* Site	0.513(1)	0.910(1)	0.362(1)	65.3(1)

According to the obtained values for the center shift (δ) and quadrupole splitting (QS) (see **Table 7**), it can be summarized that the iron in this structure is predominantly Fe^{3+} in the high spin state [25, 60-62] and that those Fe ions reside at two different crystallographic sites, each distorted octahedral sites. The spectrum and fit to the data obtained for Sr_2FeTeO_6 is consistent with that obtained for the same material by Ortega-San Martin *et al.* [25]. In addition to the two doublets fitted to their data, our spectra also clearly contain an additional component, which can be fitted by a doublet, with small shoulders at approximately +1.5 mm s^{-1} and -0.8 mm s^{-1} which were not fit in the previous study, although the presence of such a component can clearly be seen in the spectrum reproduced by Ortega-San Martin *et al.* [25]. Here, we obtained very similar shoulders in our data for the *x = 0, 0.25* and *0.50* and *0.75* samples, which we could also fit satisfactorily. These shoulders decrease in intensity with increasing *x*, such that the area decreases from approximately 14.0 % through 4.4 % to 4.2 % for *x = 0, 0.25* and *0.50*, respectively. If these shoulders are present in the spectrum for sample *x = 0.75*, they are very weak, and their area ratio approaches zero. The structural origins of this component are unclear, and we find no clear evidence for such a site from the other techniques employed in this study. With a particularly large QS of 2.062 mm s^{-1} the site is unusual for Fe^{3+} sites (indicated by its CS of 0.456 mm s^{-1}), and is thus highly distorted from cubic symmetry. Further research is required to understand the nature and origins of this minor component.

Further, in agreement with the work of Ortega-San Martin *et al.* [25], our Fe – O bond distances of ~196 pm and ~206 pm obtained from diffraction (**Table 4**) are consistent with our obtained Mössbauer CS of ~ 0.45 – 0.52 mm s^{-1}, based on the work of McCammon [52] for iron-containing perovskites.

Figure 8a shows a small increase in the center shift as iron is progressively substituted for nickel at both site *2a* and *2*d. The value of CS for all data confirms the valence of the Fe ions (+3) in both Fe sites *2a* and *2d*. The high quadrupole splitting values of *2a* site listed in **Table 7** combined with a very high splitting, most probably, indicate that *2a* site is more distorted than *2d* site with an asymmetric charge distribution of cations in *2a* site. From **Figure 8b**, the small increase of quadrupole splitting (QS) for *2a* site is explained by a variation of the electric field gradient which probably also increases with increasing Fe substitution. By contrast, the quadrupole splitting for *2d* site decreases slightly with decreasing Fe in the structure. This indicates a decrease in the electric field gradient that could be the results of a more symmetrical environment for Fe in this position (*2d* site).

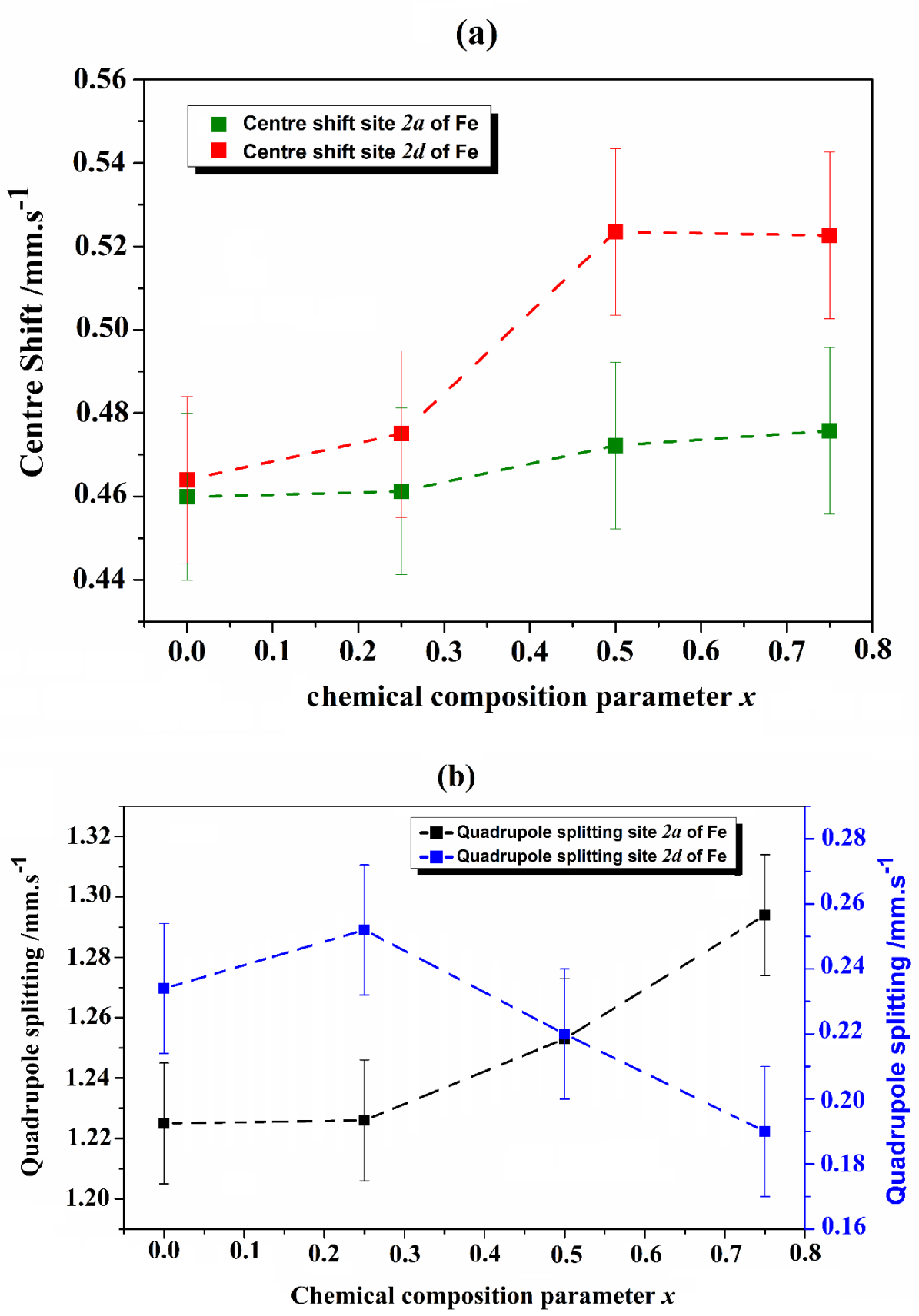

Figure 8. (a) Centre shift (CS), and **(b)** quadrupole splitting (QS) as a function of substitution level *x*.

From the refined crystal structure models, two Fe sites exist with an asymmetric distribution (of *B* cations) through these sites across the DP series (excluding *x = 0, 1*). Furthermore, the octahedral *B*-O distances from the *B* cations at the 2*d* site increase with increasing Fe content (decreasing *x*). This completely contrasts with the trend in *B*-O atomic distances from the octahedral 2*a* that decrease with decreasing Fe (increasing *x*) (see **Table 4**). Stronger interactions between cations in *B* sites and the six atoms of oxygen would increase the electric field gradient and the quadrupole splitting (QS). This premise enables site 1 to be assigned as the octahedral 2*a* in the monoclinic DP structure, whereas site 2 (as observed in the Mössbauer measurements) and be attributed to the octahedral 2*d*, which is the less distorted of the two *B*-O environments in the DP structure. Similar behavior has been reported for iron in other ferrate DP structures which also have the monoclinic structure with an anti-site effect of cations between *B* and *B'* sites, such as $ALaFeTiO_6$ (*A* = Ca, Sr, Ba) double perovskite oxide [53- 55]. Therefore, the obtained results from Mössbauer spectroscopy are consistent with the Rietveld refinement study.

3.6. Thermal analysis

The thermal behavior of this series at high temperature was investigated by TGA/DSC. The TG and DSC curves plotted in **Figure S7** show a negligible mass change for all the compositions. These results confirm the stability of our series at high temperature.

3.7. Magnetic properties

To better understand the influence of cations substitution and their ordering into *B*-sites on the magnetic properties, the molar susceptibility measurements of DP $Sr_2(Fe_{1-x}Ni_x)TeO_6$ were performed at low temperature range from 300 K down to 5 K, with an applied magnetic field of 1000 Oe in modes of zero-field cooled (ZFC) and field cooled (FC).

As shown in **Figure 9**, the data collected after cooling in zero applied field (ZFC) at 1000 Oe reached a maximum at the (spin) freezing temperature T_F (see **Table 8**). In particular, the values of T_F for *x=0* and T_N for *x = 1* at 1000 Oe are in close agreement with what was reported by Ortega-San Martin *et al.* [25] and D. Iwanaga *et al.* [30]. Interestingly, the reduction in T_F is getting strong when Fe and Ni cations are together in the structure, as well as when Ni is increasing, which indicates a strong AFM interaction due to the cation-disorder in *B*-site of DP series. This fact was explained based on the rules of Goodenough-Kanamori, which announced that the antiferromagnetic behavior is dominant when multiple types of interactions are present in the systems [56]. This confirms that Fe^{3+} ($3d^5$) ions are in HS state with t_{2g} and e_g half-filled, and Ni^{2+} ($3d^8$) ions are in HS state with t_{2g} saturated of electrons and e_g half-filled.

Moreover, we notice that for all the series, the ZFC and FC curves are irreversible (see **Figure 9**), suggesting weak ferromagnetic interactions for this series, which result from a short range of an antiferromagnetic order of the samples and/or the existence of spin glass behavior [25 and 57, 58]. The higher the *B*-site disorder, the more likely the ground state is to be a spin glass, and as mentioned above in Rietveld refinement data that the degree of order is going to be less from *x = 0* to *x = 1*, which means

that the ground state of magnetic order could prevail with decreasing Fe. Thus, the doped materials might be spin glasses or magnetically ordered. At high temperature of the paramagnetic part –exceeding T_F-, the magnetic molar susceptibility does not follow the classical Curie-Weiss law for the compositions *x = 0* and *0.25*, otherwise based on the reciprocal susceptibility the magnetic moments of these compositions are calculated at 300 K. In addition, it is observed that the curves of the inverse susceptibility of compositions *x = 0* and *0.25* are not linear, which is related to the site disorder/vacancies and complex exchange pathways of Fe^{3+} [25]. In contrast to other the compositions of *x= 0.5, 0.75* and *1*, the inverse magnetic susceptibility is fitted between 150 and 300 K to the Curie-Weiss equation $\chi_{mol} = C/T-\theta_{CW}$ (see **Figure S8** which represents the temperature dependence of inverse susceptibility). A decrease in Weiss temperatures (Tc = θ) is noticed when *x* increases. All derived magnetic parameters from the Curie-Weiss fits including the Weiss temperatures (θ), the effective magnetic moments, and the frustration factor are summarized in the **Table 8**. Negative values of Weiss temperatures for the compositions *x = 0.25, 0.5, 0.75* and *1* are obtained, indicating a strong antiferromagnetic interaction between the *3d* cations. This temperature decreases monotonically as *x* increases. The frustration factor is calculated for all the series based on the ratio $|\theta|/T_N$ and it showed a strong frustration for the samples *x = 0.5* and *0.75* signaling a highly frustrated behavior of the exchange interactions [59]. The factor that can caused such high values of frustration in the spins at low temperature is the high degree of disorder in *B*-site, and a complex exchange interaction existing between *3d* cations may also be the reason

The effective magnetic moments for samples *x = 0* and *1* are in excellent agreement with references [25, 30]. Besides, they are equal to the theoretical magnetic moments considering the spin value of Fe^{3+} for composition *x=0* and only Ni^{2+} for composition *x=1*. As the magnetic moment is strongly related to the spin-state of Fe, the low values of the obtained effective paramagnetic moments observed for x = 0.5 and x = 0.75 could be explained by a spin-state transition of Fe^{3+} from HS to LS.

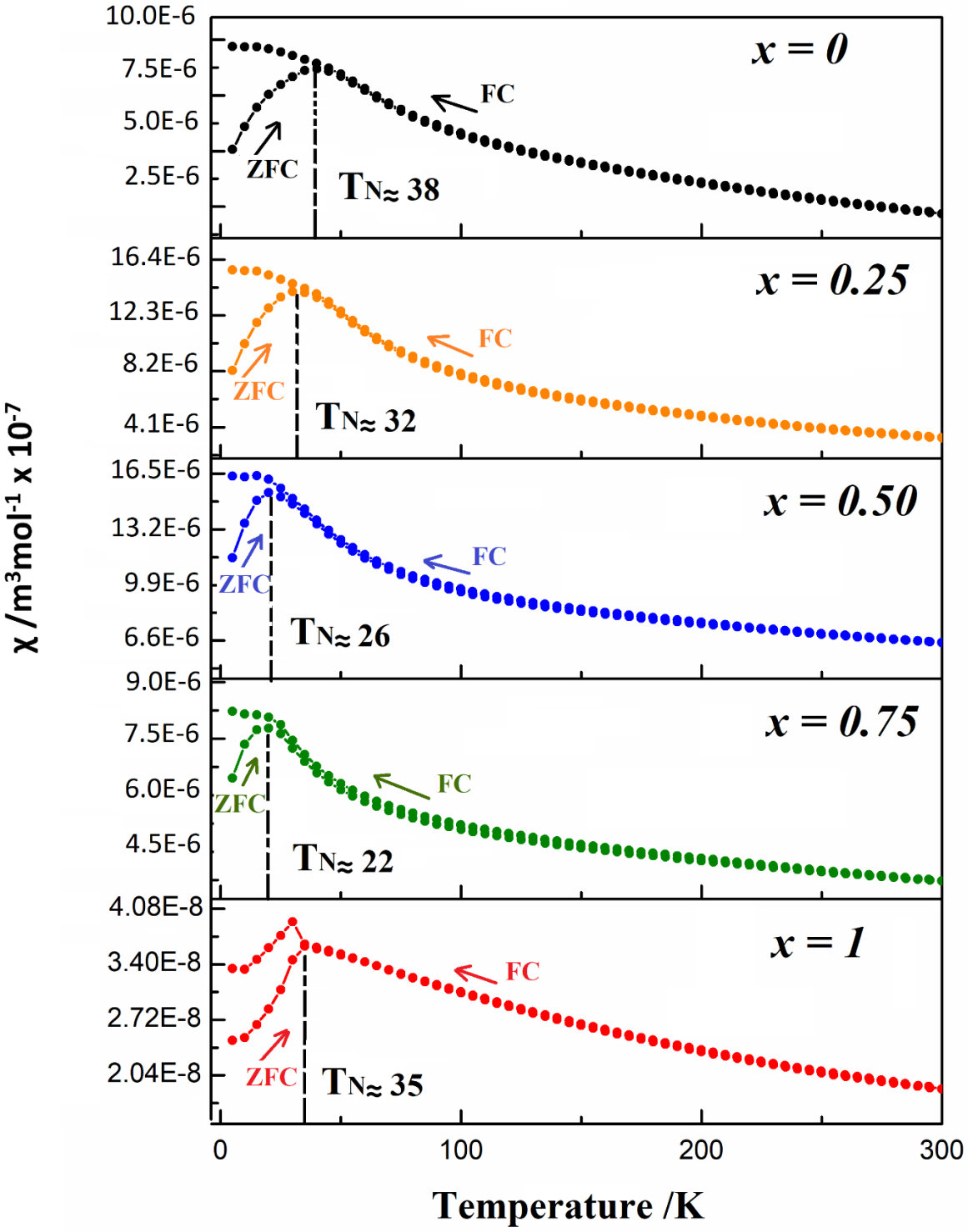

Figure 9: The temperature dependence of the susceptibility carried out in zero field cooled (ZFC) and field cooled (FC) modes at the magnetic field 1000 Oe.

Table 8. Summary of magnetic parameters of DP $Sr_2(Fe_{1-x}Ni_x)TeO_6$.

Composition *x*:	Weiss temperature Θ /K	Effective magnetic moment μ_{eff} /μ_B	The Néel temperature T_N /K	Frustration parameter $f = \lvert-\theta\rvert / T_N$

0	91 (at T = 300 K)	$\mu_{(T = 300\ K)} \approx 5.58$	≈ 38	≈ 2.39
0.25	≈ -12.5	≈ 2.43	≈ 31	≈ 0.40
0.5	≈ -337.5	≈ 1.52	≈ 24.9	≈ 13.55
0.75	≈ -450	≈ 1.23	≈ 20	≈ 22.5
1	≈ -225	≈ 2.3	≈ 35	≈ 6.42

4. CONCLUSION

This investigation provides a systematic study of the structural and spectroscopic properties of the double perovskite series $Sr_2(Fe_{1-x}Ni_x)TeO_6$ (*x = 0, 0.25, 0.50, 0.75* and *1*). The refined crystal structures demonstrate that all the members of the series are isostructural, forming a solid solution in monoclinic space group *I2/m*. The data further establish that the d-block and p-block metal cations (iron, nickel and tellurium) are disordered across the two available DP *B*-sites (with site symmetry 2*a* and 2*d*). Nevertheless, there is a preference for Te to occupy the octahedral 2*a* site just as in Sr_2NiTeO_6, which has a completely ordered *B* cation distribution. This fact is due to the significant contrast in ionic charge for –nickel (iron) and tellurium (as opposed to the closer similarity between the ionic charge or iron and nickel species). The impact of replacing iron with nickel was observed from the evolution of the BO_6 octahedral distortion with *x*. This effect was noticeable (and somewhat predictable) from the diminishing tolerance factor values as the nickel content increases., Experimentally, this was also manifest in the increasing frequency of the Raman band located at 750 cm^{-1} with *x* and the occurrence of a splitting of the Raman band located at 550 cm^{-1}. DR-UV-Vis results indicated an increase in the band gap energies with a direct optical transition types for all the samples as iron is substituted by nickel. The center shift obtained from Mössbauer measurements performed at room temperature reveals the presence of Fe^{3+} in a high-spin state in an octahedral environment. Further, the quadrupole splitting increases as more nickel is introduced into the structure. By reference to the structural data, this quadrupolar splitting reflects a strong correlation between the hyperfine parameters and the anti-site disorder of Fe-Ni-Te cations in the *B*-sites of the monoclinic DP structure. The magnetic measurements reveal the existence of a short strong antiferromagnetic behavior, and at low temperature of around 20 K, this series is showing a spin glass character. Further work is now in progress using variable temperature powder neutron diffraction and magnetometry to allow a more complete rationalization of extended structure, cation distribution, electronic structure, and magnetism.

5. Acknowledgments

AZ gratefully acknowledged the Deutsche Forschungsgemeinschaft (DFG) for financial support through ZA 1170/1-1. The authors thank University of Bremen, and University of Glasgow for assistance with the experimental work. Our sincere thanks to Prof. Mark Murrie[2] and Dr. Lucy Smythe[2] for performing the SQUID measurements. We would like to thank Dr. Alex Scrimshire[6] for collecting Mössbauer data.

One of the authors, JM Igartua, acknowledges the support from the project Nº IT-1714-22 Gobierno Vasco.

Author contributions: All the authors have accepted responsibility for the entire content of this submitted manuscript and approved submission.

Research funding: This work was supported by Deutsche Forschungsgemeinschaft (DFG) through ZA 1170/1-1.

Conflict of interest statement: The authors declare no conflicts of interest regarding this article.

6. REFERENCES

[1]. S-D. Tanusri, *Mater. Res. Express*, 2020, 7, 014003.

[2]. A. Paul and T. Birol, *Phys. Rev. Research*, 2020, *2*, 033156.

[3]. S. Vasala, M. Karppinen, *Prog. Solid State Chem.*, 2015, 43, 1-36.

[4]. K. Leng, Q. Tang, Y. Wei, L. Yang, Y. Xie, Z. Wu, and X. Zhu, *AIP Advances*, 2020, 10(12), 120701.

[5]. W. Yin, B. Weng, J. Ge, D. Q. sun, Z. Li and Y. Yan, *Energy Environ. Sci.*, 2019, 12, 442-462.

[6]. S. A. Mir and D.C. Gupta, *Scientific Reports*, 2021, 11(1).

[7]. A. S. Thind, S. Kavadiya, M. Kouhnavard, R. Wheelus, S. B. Cho, L.-Y. Lin, C. Kacica, H. K. Mulmudi, K. A. Unocic, A. Y. Borisevich, G. Pilania, P. Biswas, and R. Mishra, *Chem. Mater.*, 2019, 31, 4769−4778.

[8]. T. Maiti, M. Saxena, and P. Roy, *J. Mater. Res.*, 2018, 34 (1), 107-125.

[9]. F. Zaza, S. Bonanni, and E. Serra, *2020 IEEE International Workshop on Metrology for Industry* 4.0 & IoT, 2020, 685-689.

[10]. Y. Moritomo, N. Shimamoto, S. Xu, A. Machida, E. Nishibori, M. Takata, M. Sakata and A. Nakamura, *Jpn. J. Appl. Phys.*, 2001, 40, 7A, L672-L674.

[11]. A. M. Idris, T. Liu, J. Hussain Shah, A. S. Malik, D. Zhao, H. Han, and C. Li, *ACS Appl. Mater. Interfaces*, 2020, 12, 23, 25938–25948.

[12]. K. Samanta and T. Saha-Dasgupta, *Phys. Rev. B*, 2017, 95, 235102.

[13]. I. A. Gorodea, *Acta chem. IASI*, 2014, 22-2, 145-154.

[14]. G. King and P. M. Woodward, *J. Mater. Chem.*, 2010, 20, 5785–5796.

[15]. M. T. Anderson, K. B. Greenwood, G. A. Taylor, and K. R. Poeppelmeier, *Prog. Solid State Chem.*, 1993, 22, 197-233.

[16]. F. Galasso and W. Darby, *J. Phys. Chem.*, 1962, 66, 1, 131–132.

[17]. D. M. Arciniegas Jaimes, J. M. De Paoli, V. Nassif, P. G. Bercoff, G. Tirao, R. E. Carbonio, and F. Pomiro, *Inorg. Chem.*, 2021, 60(7), 4935–4944.

[18]. A. Zaraq, B. Orayech, J. M. Igartua, and A. El Bouari, *Powder Diffr.*, 2019, 34 (S1), S48-S58.

[19]. K. Ishida, C. Tassel, D. Watabe, H. Takatsu, C. M. Brown, G.Jan Nilsen, and H. Kageyama, *Inorg. Chem.*, 2021, 60 (11), 8252-8258.

[20]. B. Orayech, L. Ortega-San-Martín, I. Urcelay-Olabarria, L. Lezama, T. Rojo, María I. Arriortua, and J. M. Igartua, *Dalton Trans.*, 2016, 45, 14378-14393.

[21]. A. Zaraq, B. Orayech, J.M. Igartua, and A. El bouari, *J. Electron. Mater.*, 2019, 48 (8), 4866-4876.

[22]. Y. Wang, Y. Zhao, S. Ma, X. Li, D. Tan, J. Feng, Junxiu Liu, and B. Chen, *J. Phys. Chem. C,* 2021, 125, 45, 25253–25260.

[23]. A. Zaraq, B. Orayech, A. Faik, J.M. Igartua, A. Jouanneaux, A. El Bouari, *Polyhedron*, 2016, 110, 119–124, 0277-5387.

[24]. Á. M. Arévalo-López, E. Solana-Madruga, C. Aguilar-Maldonado, C. Ritter, O. Mentré and J. P. Attfield, *Chem. Commun.*, 2019, 55, 14470-14473.

[25]. L. Ortega-San Martin, Jon. P. Chapman, L. Lezama, José J. Saiz Garitaonandia, J. Sánchez Marcos, J. Rodríguez-Fernández, M. I. Arriortua and T. Rojo, *J. Mater. Chem.*, 2006, 16, 66-76.

[26]. L. Ortega-San Martin, J. P. Chapman, E. Hernández-Bocanegra, M. Insausti, M. I. Arriortua, and T. Rojo, *J. Phys. Condens. Matter*, 2004, 16(23), 3879–3888.

[27]. M. S. Augsburger, M. C. Viola, J. C. Pedregosa, A. Munoz, J. A. Alonso and R. E. Carbonio, *J. Mater. Chem.*, 2005, 15, 993–1001.

[28]. W.T. Fu, Y.S. Au, S. Akerboom, D.J.W. IJdo, *J. Solid State Chem.*, 2008, 181, 2523– 2529.

[29]. L. Ortega-San Martin, J. P. Chapman, G. Cuello, J. Gonzalez-Calbet, M. I. Arriortua, and T. Rojo, *Z. Anorg. Allg. Chem.*, 2005, 631, 2127-2130.

[30]. D. Iwanaga, Y. Inaguma, M. Itoh, *Mater. Res. Bull*., 2000, 35, 449–457.

[31]. J. Khatua, T. Arh, Shashi B. Mishra, H. Luetkens, A. Zorko, B. Sana, M. S. Ramachandra Rao, B. R. K. Nanda, P. Khuntia, *Scientific Reports*, 2021, 11, 6959.

[32]. J. Rodriguez-Carvajal, 1997, "Fullprof, Program for Rietveld refinement," Laboratoire Léon Brillouin (CEA-CNRS), Saclay, France.

[33]. T. Roisnel, and J. Rodriguez-Carvajal, "WinPLOTR: a Windows tool for powder diffraction pattern analysis," *Mater. Sci. Forum.*, 2001, 378–381, 118–123.

[34]. K. Momma and F. Izumi, *J. Appl. Cryst.*, 2008, 41, 653–658.

[35]. V. M. Goldschmidt, Die gesetze der krystallochemie. *Naturwissenschaften*, 1926, 14, 477–485.

[36]. K. Lagarec and R. D. G.; Version 1.0 ed.; Department of Physics, University of Ottawa: 1998.

[37]. A. M. Glazer, *Acta Cryst.*, 1975, A31, 756.

[38]. A. R. Denton and N. W. Ashcroft, *Phys. Rev. A*, 1991, 43(6), 3161–3164.

[39]. J. Bijelić, D.Tatar, S. Hajra, M. Sahu, S. J. Kim, Z. Jagličić, and I. Djerdj, *Molecules*, 2020, 25(17), 3996.

[40]. E. Kroumova, M. I. Aroyo, J. M. Perez-Mato, A. Kirov, C. Capillas, S. Ivantchev, H. Wondratschek, *Phase Transit.*, 2003, 76 155. http://www.cryst.ehu.es/.

[41]. A.P. Ayala, I. Guedes, E.N. Silva, M.S. Augsburger, M.C. del Viola, and J.C. Pedregosa, *J. Appl. Phys.*, 2007, 101, 123511.

[42]. A. Kumar, R. Shukla, A. Pandey, S. Dalal, M. Miryala, K. Ueno, M. Murakami, and R. S. Dhaka *J. Appl. Phys.*, 2020, 128(2), 025303.

[43]. V. S. Bhadram, D. Swain, R. Dhanya, M. Polentarutti, A. Sundaresan and C. Narayana, *Mater. Res. Express*, 2014, 1, 026111.

[44]. R. L. Andrews, A. M. Heyns, P. M. Woodward, *J. Name*., 2013, 00, 1-3.

[45]. J. Tauc, *Mater. Res. Bull*., 1968, 3, 1, 37-46.

[46]. J. Tauc, A. Menth *J. Non-Cryst. Solids*, 1972, 8-10, 569–585.

[47]. A. Kirsch, M. M. Murshed, M. Schowalter, A. Rosenauer, and T. M. Gesing, *J. Phys. Chem. C*, 2016, 120, 33, 18831-18840.

[48]. Th. M. Gesing, M. M. Murshed, S. Schuh, O. Thüringer, K. Krämer, T. Neudecker, C. B. Mendive, L. Robben, *J. Mater. Sci.*, 2022.

[49]. Y. A. Alsabah, A. T. Elden, M. S. AlSalhi, A. A. Elbadawi, M. A. Siddig, *Results in phys.*, 2019, 15, 102589.

[50]. Y. A. Al sabah, M. S. AlSalhi, A. A. Elbadawi, E. M. Mustafa, *Materials* (Basel), 2017, 10(5):469.

[51]. F. I. H. Alias, R. Rajmi, M. F. Maulud and Z. Mohamed, *RSC Adv*., 2021, 11, 31631.

[52]. C. McCammon, *Ph. Transit*., 1996, 58(1-3), 1-26.

[53]. P. Adler, S. A. Medvedev, P. G. Naumov, S. Mohitkar, R. Rüffer, M. Jansen, and C. Felser, *Phys. Rev. B*, 2019, 99, 13.

[54]. A. A. Elbadawi, O.A. Yassin, A. A. Gismelseed, *J. Magn. Magn. Mater*., 2013, 326, 1-6.

[55]. A. El Hachmi, B. Manoun, Y. Tamraoui, S. Louihi, L. Bih, M. Sajieddine, and P. Lazor, *J. Struct. Chem*., 2020, 61, 6, 861-872.

[56]. S. Jana, P. Aich, P. A. Kumar, O. K. Forslund, E. Nocerino, V. Pomjakushin, M. Månsson, Y. Sassa, P. Svedlindh, O. Karis, V. Siruguri and S. Ray, *Sci. Rep*., 2019, 9, 18296.

[57]. Ajay Kumar and R. S. Dhaka, *Phys. Rev. B*, 2020, 101, 094434.

[58]. A. K. Kundu, V. Pralong, V. Caignaert, C. N. R. Rao and B. Raveau, *J. Mater. Chem*., 2007, 17, 3347-3353.

[59]. K. Ishida, C. Tassel, D. Watabe, H. Takatsu, C.M. Brown, G. J. Nilsen, and H. Kageyama, *Inorg. Chem*., 2021, 60, 8252-8258.

7. SUPPLEMENTARY INFORMATION

Table S1 : EDX results for the elements of double perovskite series $Sr_2(Fe_{1-x}Ni_x)TeO_6$

Elements	Sr_2FeTeO_6	$Sr_2(Fe_{0.75}Ni_{0.25})TeO_6$	$Sr_2(Fe_{0.50}Ni_{0.50})TeO_6$	$Sr_2(Fe_{0.25}Ni_{0.75})TeO_6$	Sr_2NiTeO_6
	Atomic %	Atomic %	Atomic %	Atomic %	Atomic %
O K	62.47(4)	63.03(4)	64.04(4)	56.55(3)	63.5(4)
Fe K	8.65(3)	6.16(5)	3.78(3)	2.39(3)	-
Ni K	-	1.76(3)	3.45(5)	10.42(3)	9.8(5)
Te L	9.29(3)	9.37(3)	8.91(3)	13.09(3)	8.56(3)
Sr L	19.59(4)	19.68(4)	19.82(4)	17.55(4)	18.14(4)

7.1. Rietveld refinement plots:

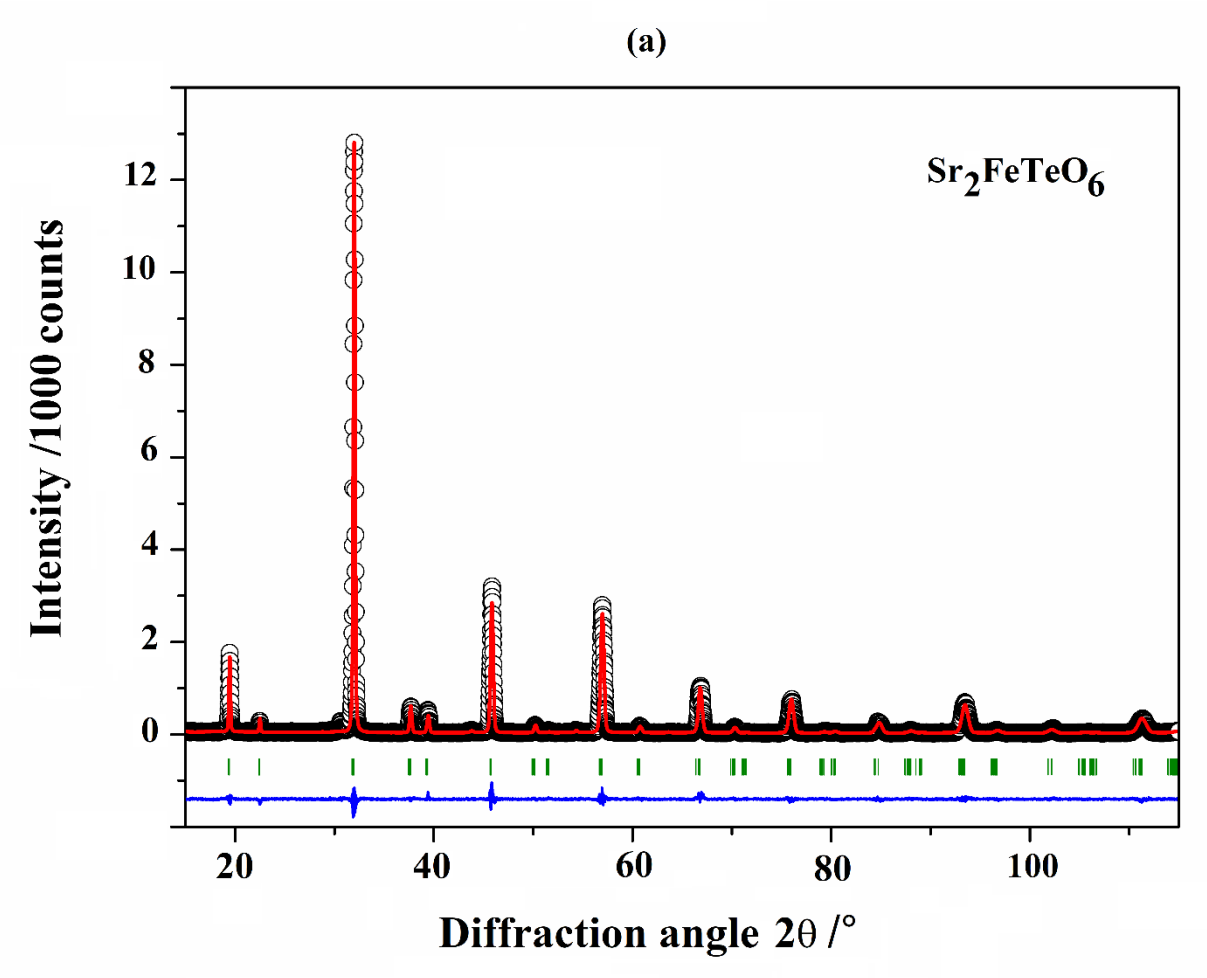

(b)

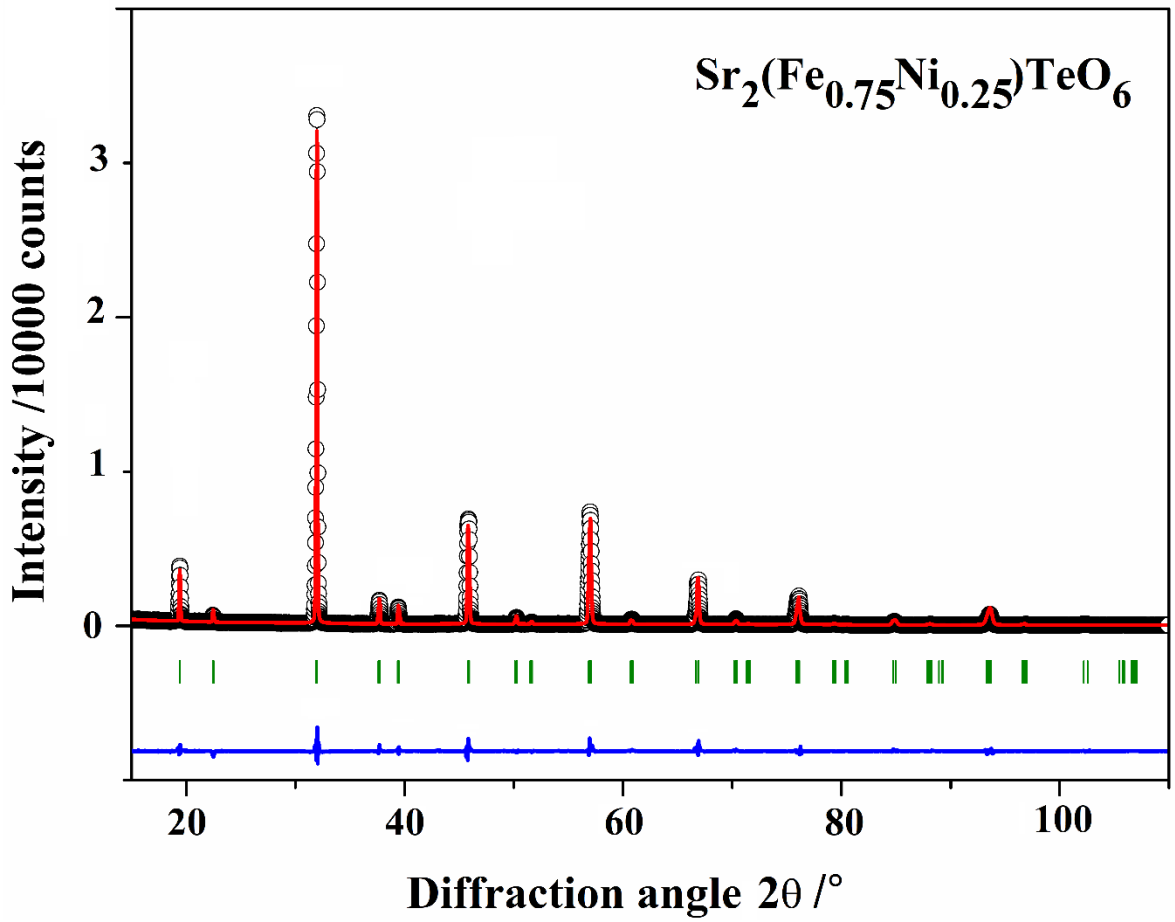
Sr2(Fe0.75Ni0.25)TeO6
Intensity /10000 counts
3
2
1
0
20
40
60
80
100
Diffraction angle 2θ /°

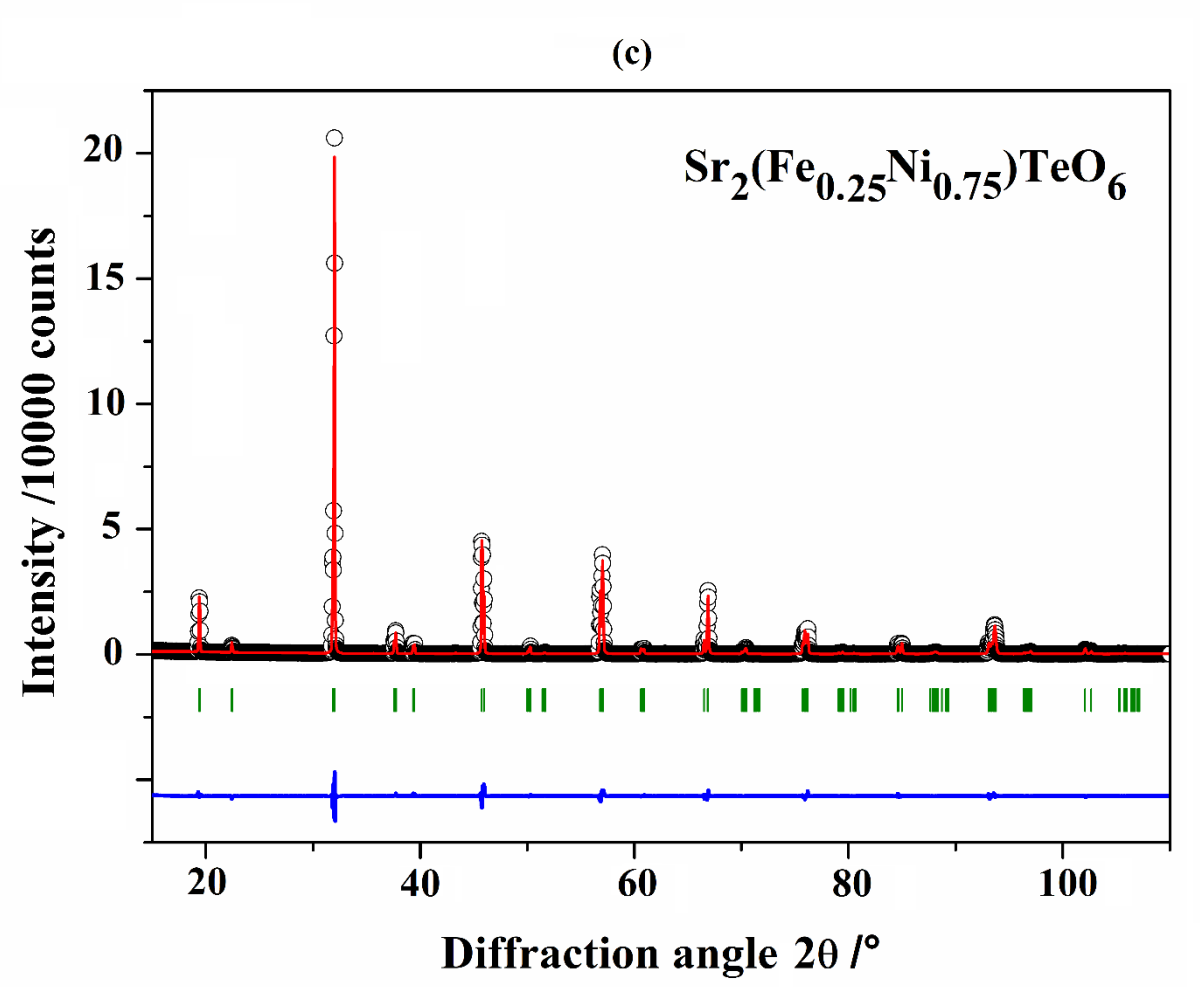
(c)
Sr2(Fe0.25Ni0.75)TeO6
Intensity /10000 counts
20
15
10
5
0
20
40
60
80
100
Diffraction angle 2θ /°

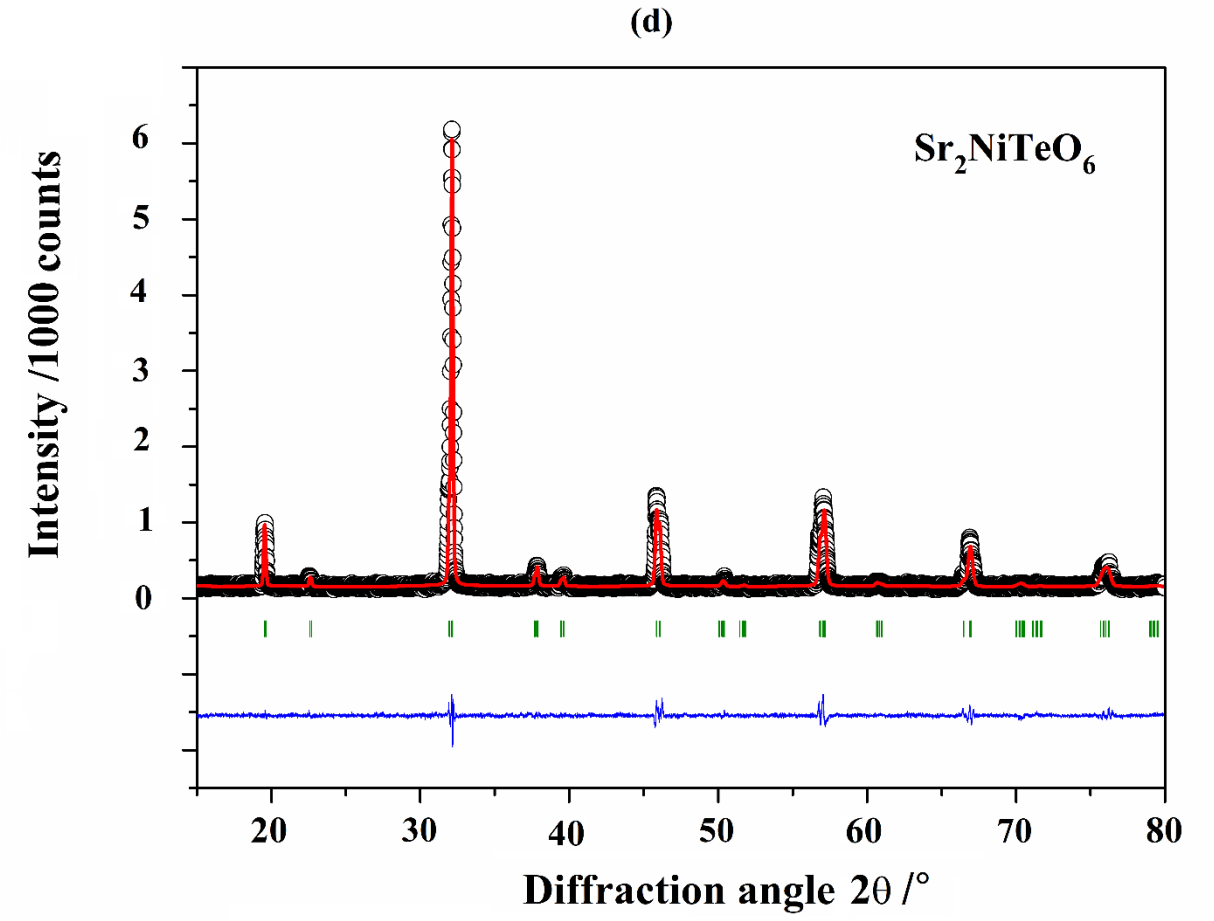

Figure S1: Rietveld refinement profiles for the compositions **(a)** *x = 0*, **(b)** *0.25*, **(c)** *x = 0.75 and* **(d)** *x = 1*. The experimental circles (black), calculated pattern (red) and difference profile (blue). Vertical green markers indicate the respective DP Bragg reflections.

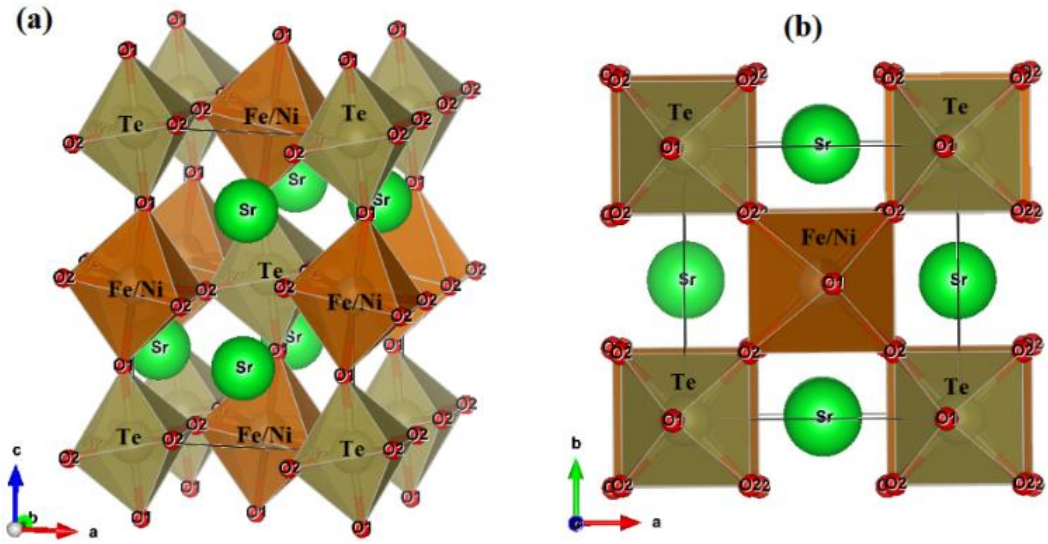

Figure S2: Crystal structures of double-perovskites $Sr_2(Fe_{1-x}Ni_x)TeO_6$. The unit cell in a perspective view **(a)** and projected in the (001) direction **(b)** showing the tilt system ($a^-a^-c^0$) is given.

7.2. SEM analysis

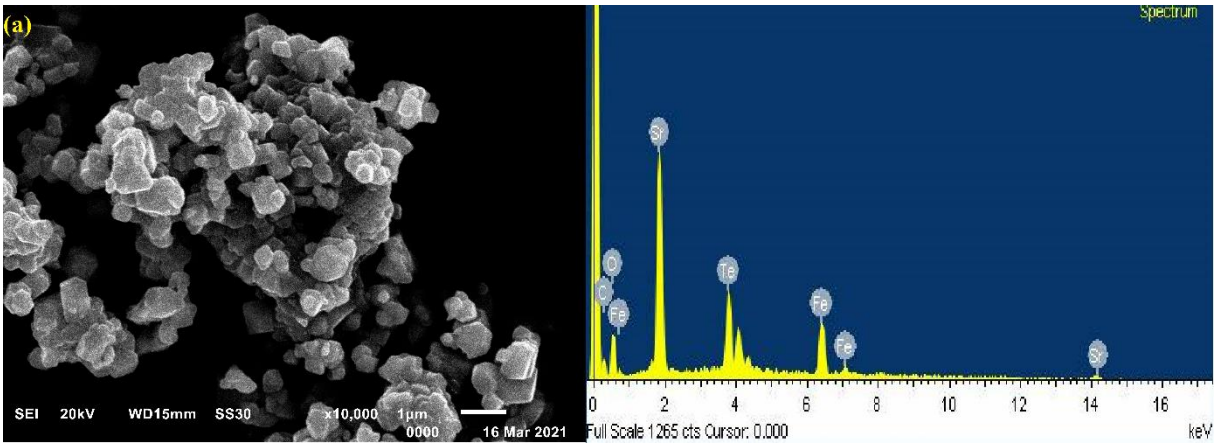
(a)
SEI 20kV WD15mm SS30 x10,000 1μm 0000 16 Mar 2021
Spectrum
Sr
O
C
Fe
Te
Fe
Fe
Sr
0 2 4 6 8 10 12 14 16
Full Scale 1265 cts Cursor: 0.000
keV

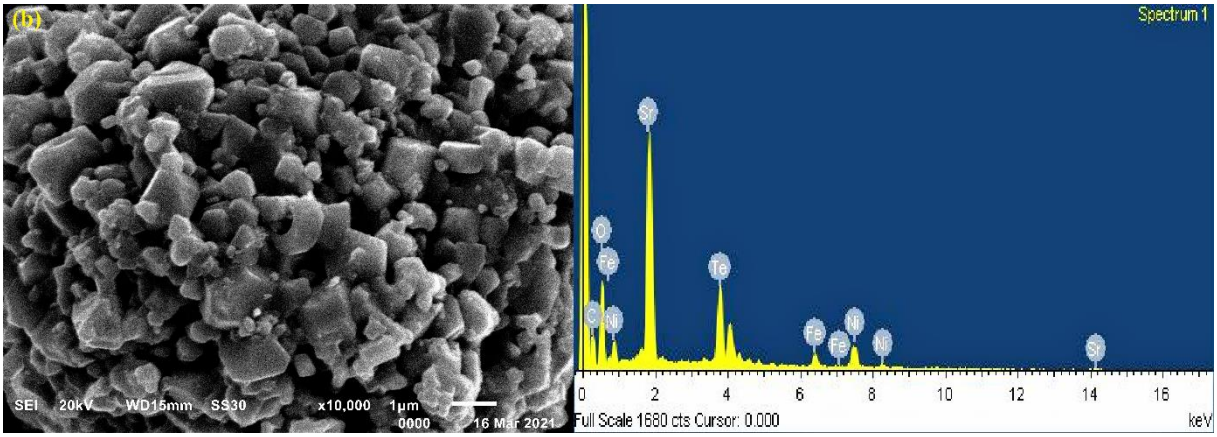
(b)
SEI 20kV WD15mm SS30 x10,000 1μm 0000 16 Mar 2021
Spectrum 1
Sr
O
Fe
Te
C
Ni
Fe
Fe
Ni
Ni
Sr
0 2 4 6 8 10 12 14 16
Full Scale 1680 cts Cursor: 0.000
keV

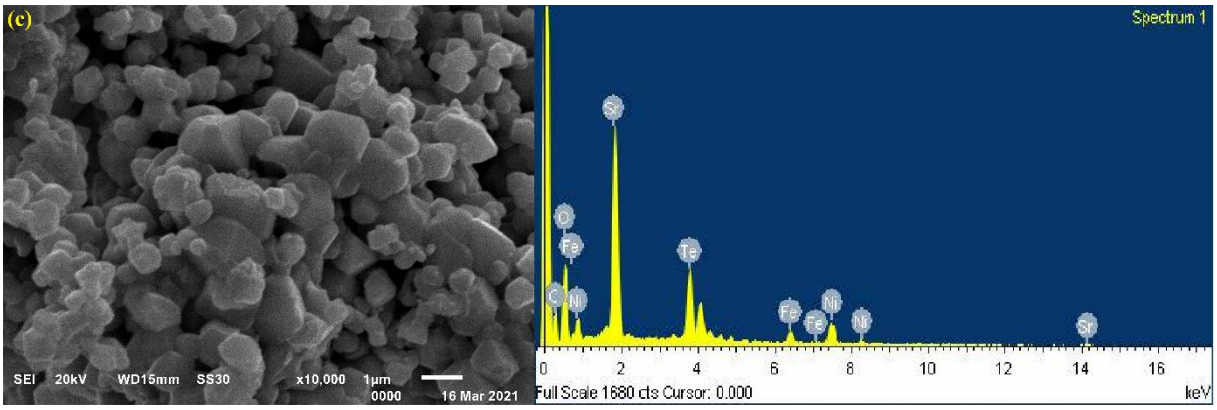
(c)
SEI 20kV WD15mm SS30 x10,000 1μm 0000 16 Mar 2021
Spectrum 1
Sr
O
Fe
Te
C
Ni
Fe
Fe
Ni
Ni
Sr
0 2 4 6 8 10 12 14 16
Full Scale 1680 cts Cursor: 0.000
keV

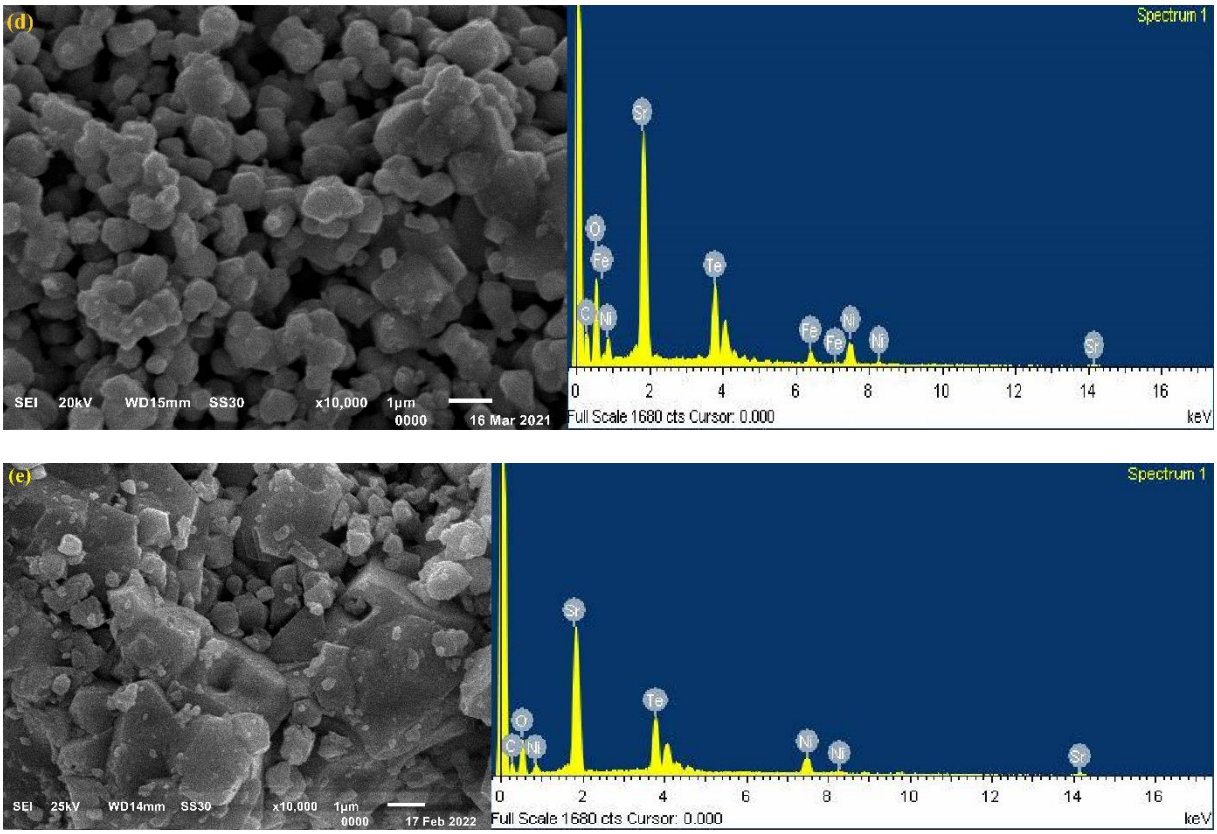

Figure S3 : SEM images and corresponding EDX spectra for the double perovskite series $Sr_2(Fe_{1-x}Ni_x)TeO_6$: (**a**) Sr_2FeTeO_6, (**b**) $Sr_2Fe_{0.75}Ni_{0.25}TeO_6$, (**c**) $Sr_2Fe_{0.5}Ni_{0.5}TeO_6$, (**d**) $Sr_2Fe_{0.25}Ni_{0.75}TeO_6$ and (**e**) Sr_2NiTeO_6.

7.3. Raman spectra fitting

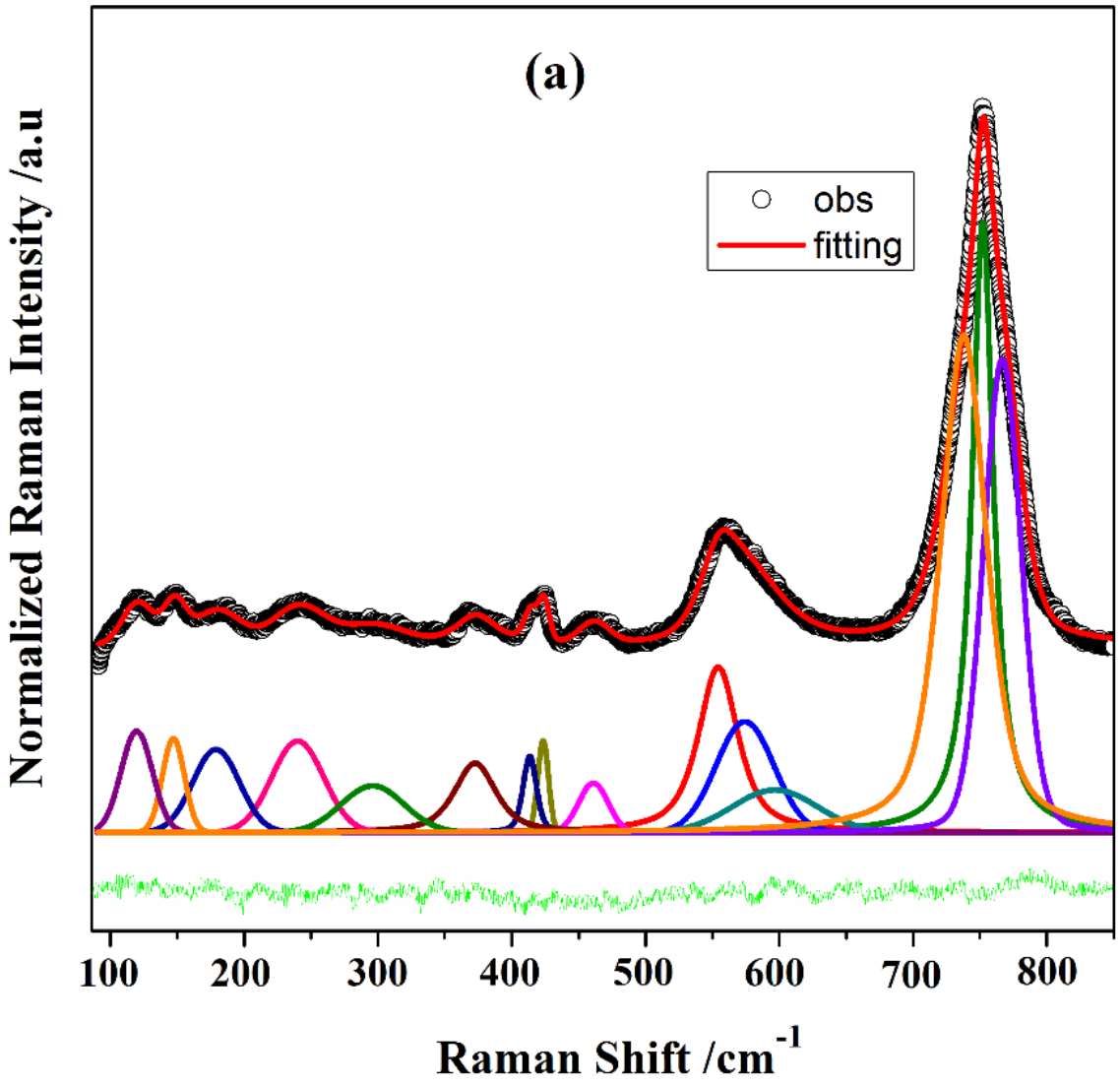
(a)
obs
fitting
Normalized Raman Intensity /a.u
100
200
300
400
500
600
700
800
Raman Shift /cm-1

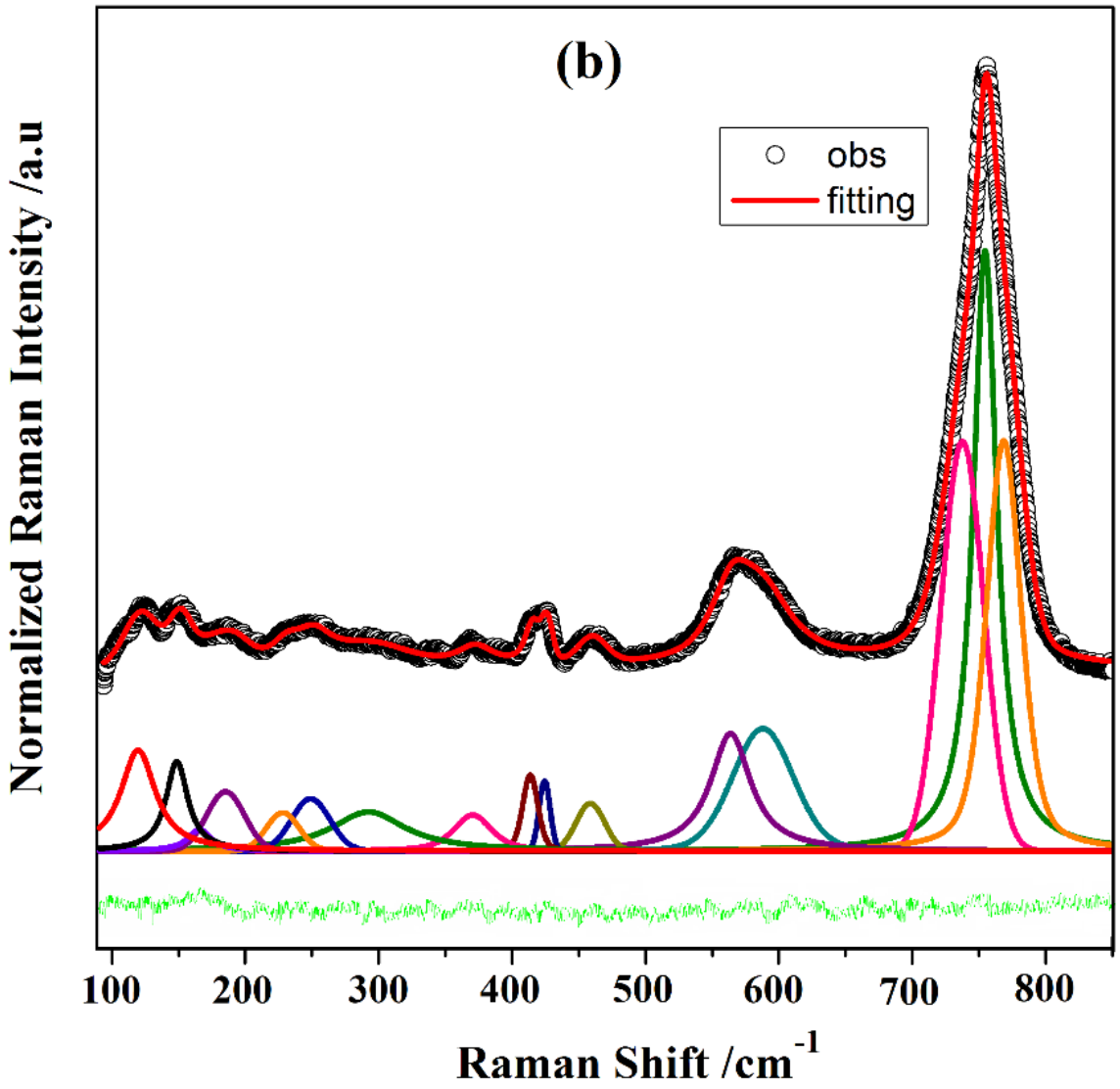
(b)
obs
fitting
Normalized Raman Intensity /a.u
100
200
300
400
500
600
700
800
Raman Shift /cm-1

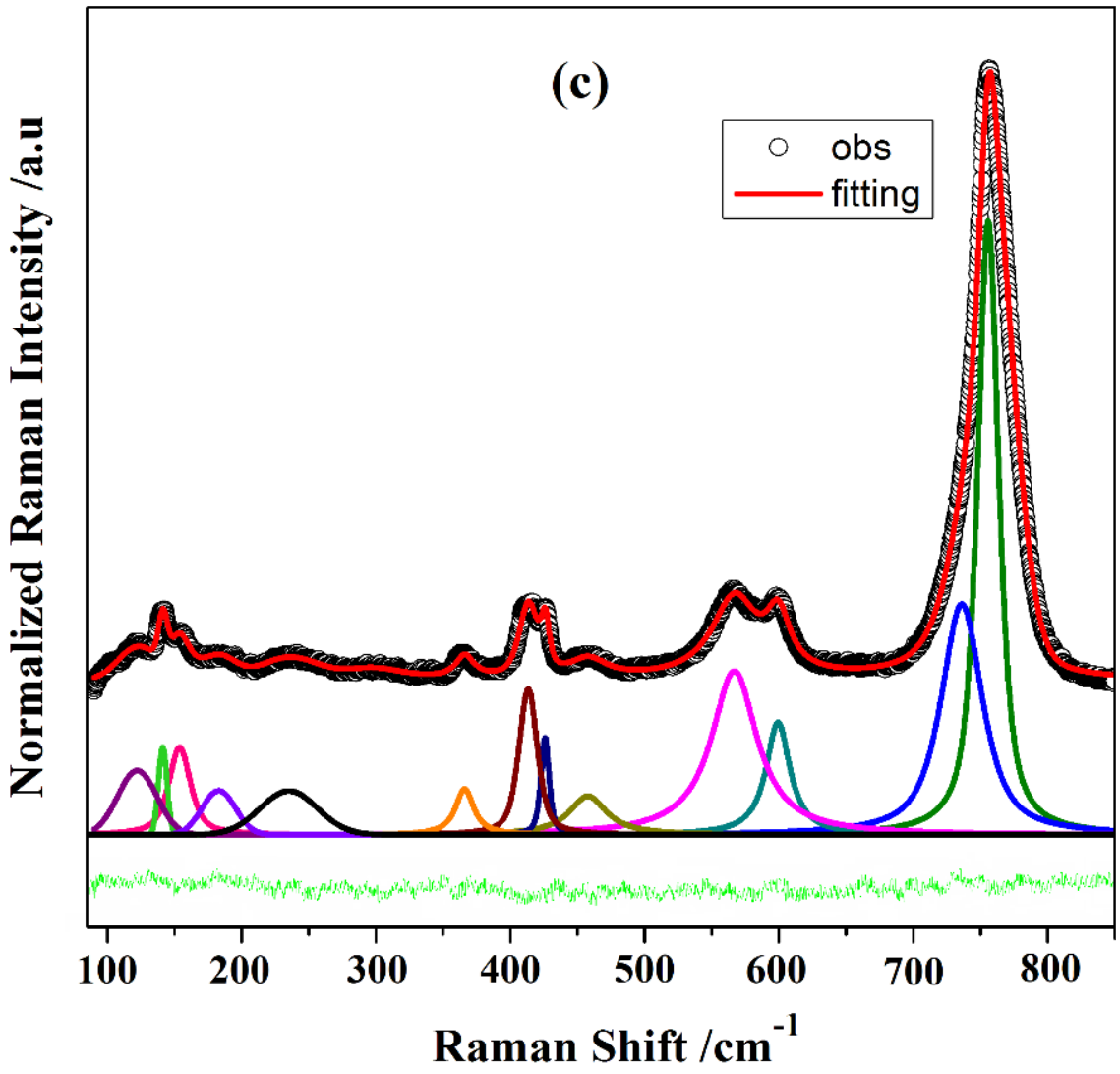
(c)
obs
fitting
Normalized Raman Intensity /a.u
100
200
300
400
500
600
700
800
Raman Shift /cm-1

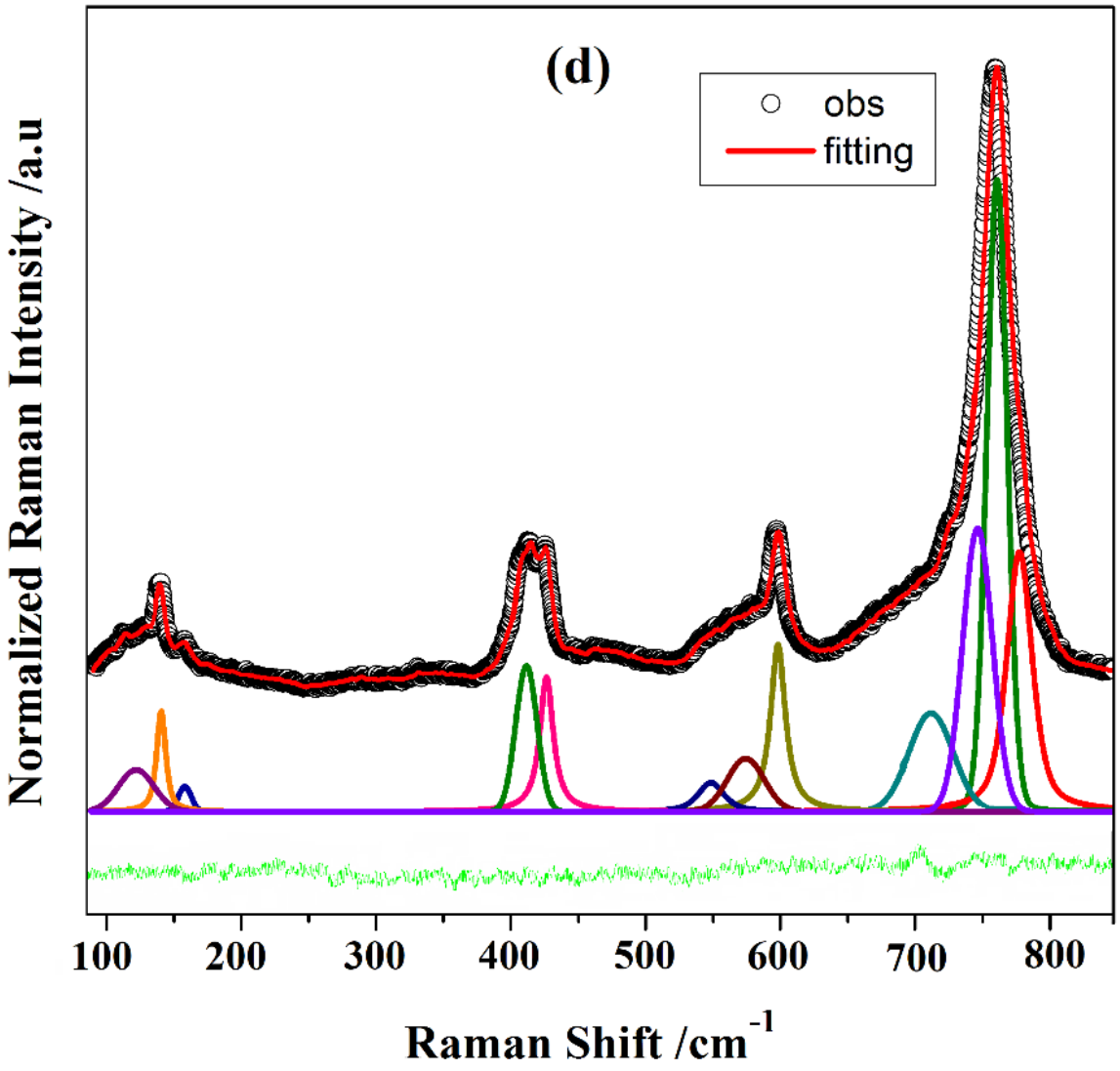

Figure S4 : Lorentzian fitting of Raman data for the composition (**a**) $Sr_2Fe_{0.75}Ni_{0.25}TeO_6$, (**b**) $Sr_2Fe_{0.50}Ni_{0.50}TeO_6$, (**c**) $Sr_2Fe_{0.25}Ni_{0.75}TeO_6$, and (**d**) Sr_2NiTeO_6 at room temperature.

7.4. Tauc and DASF plots

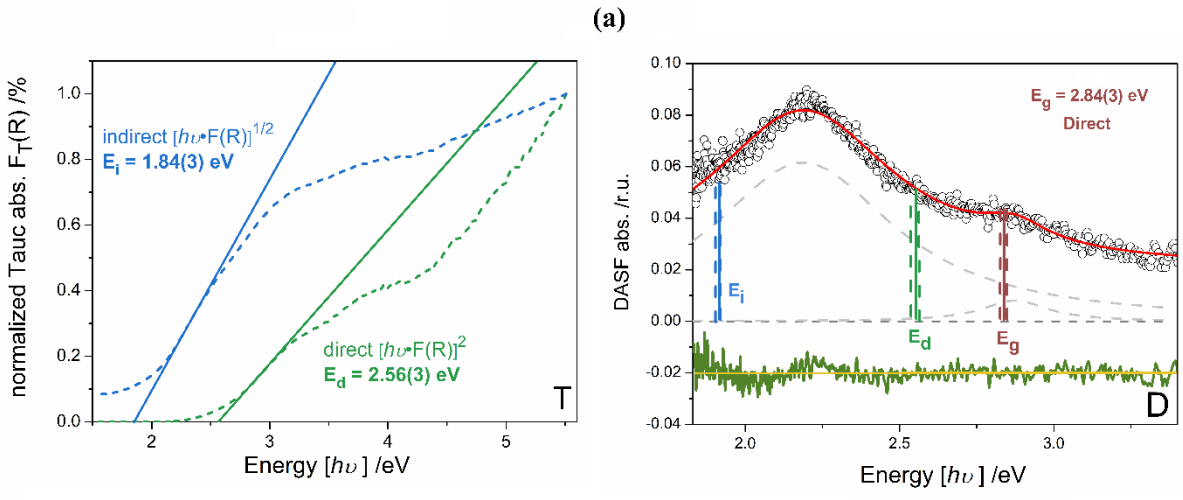

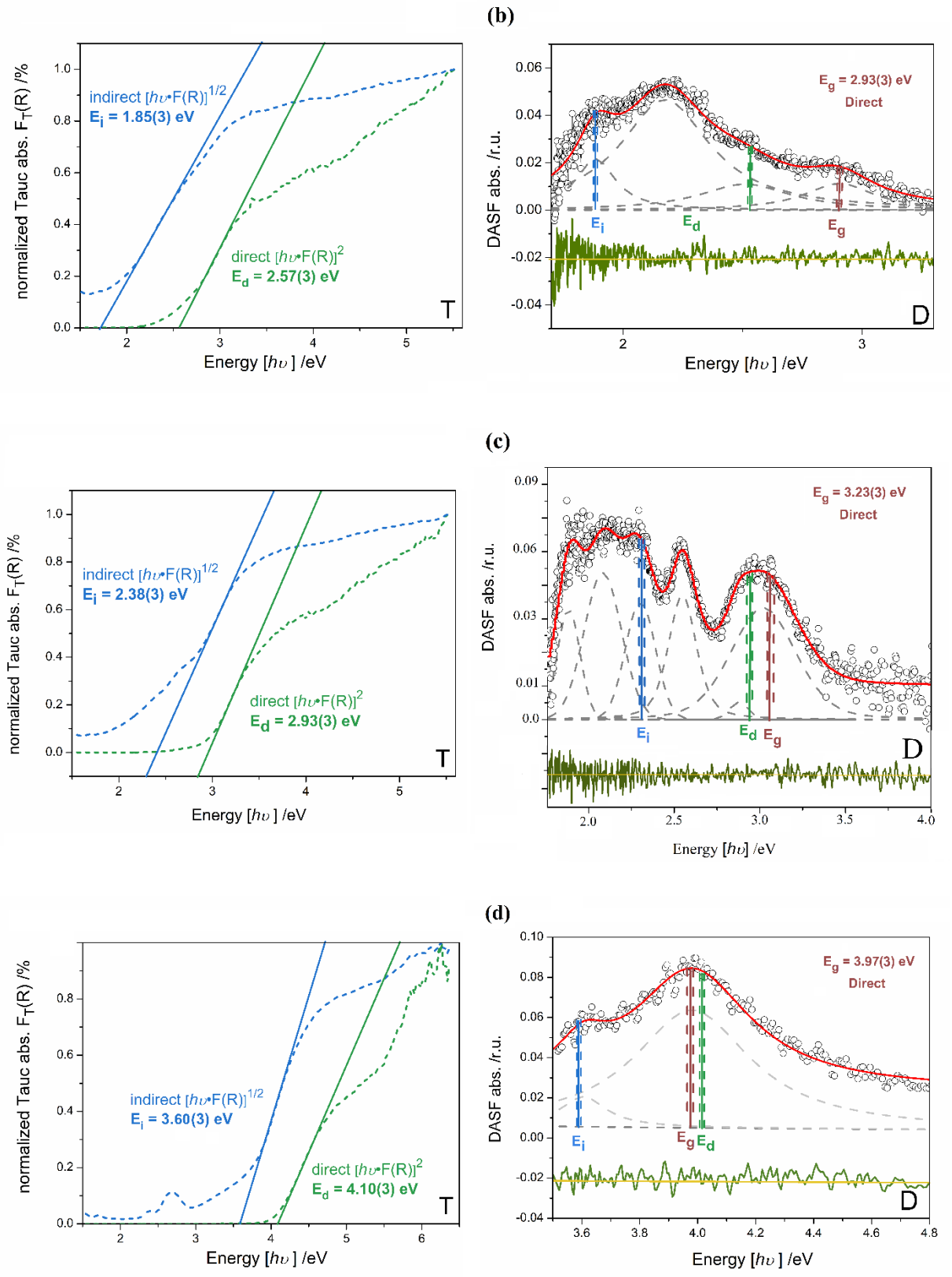

Figure S5 : Tauc plots for direct $(h\upsilon * F(R))^2$ and indirect $(h\upsilon * F(R))^{1/2}$ transitions (left) and DASF plots (right) for the series of compositions : (**a**) $Sr_2(Fe_{0.75}Ni_{0.25})TeO_6$, (**b**) $Sr_2(Fe_{0.50}Ni_{0.50})TeO_6$, (**c**) $Sr_2(Fe_{0.25}Ni_{0.75})TeO_6$, and (**d**) Sr_2NiTeO_6.

7.5. ^{57}Fe Mossbauer spectroscopy

(a)

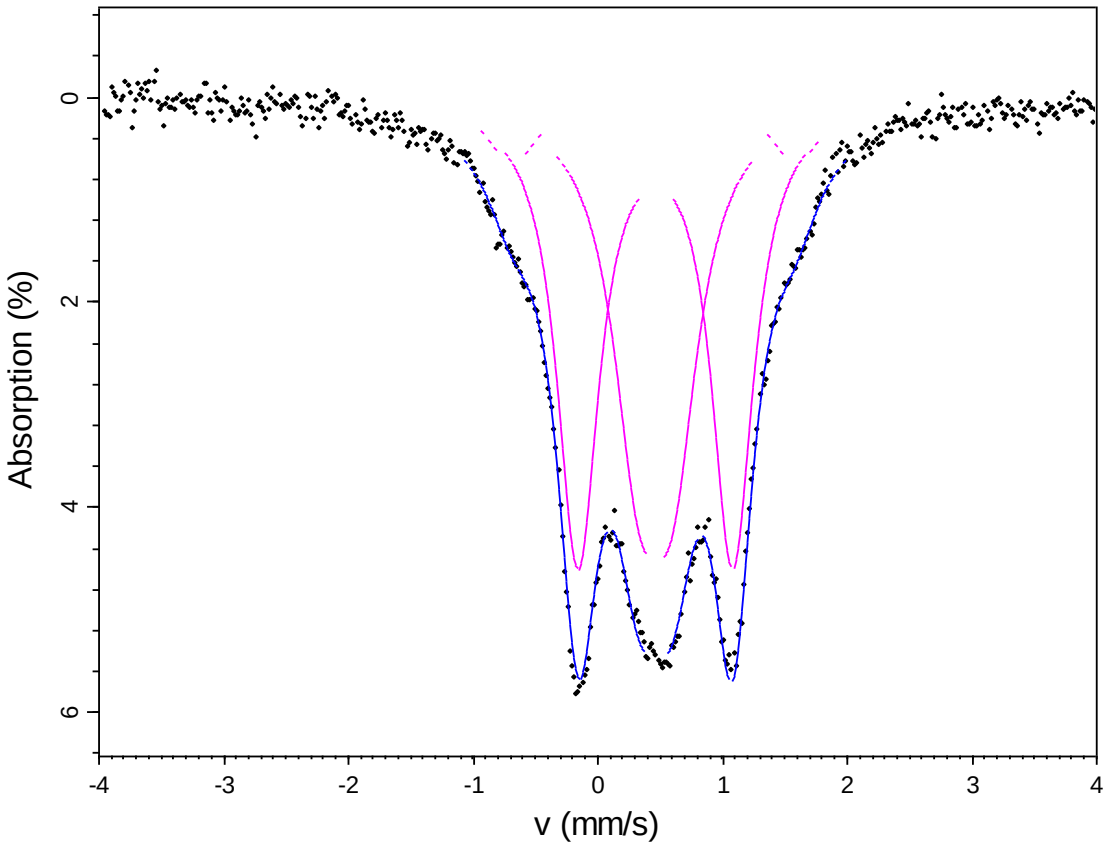

(b)

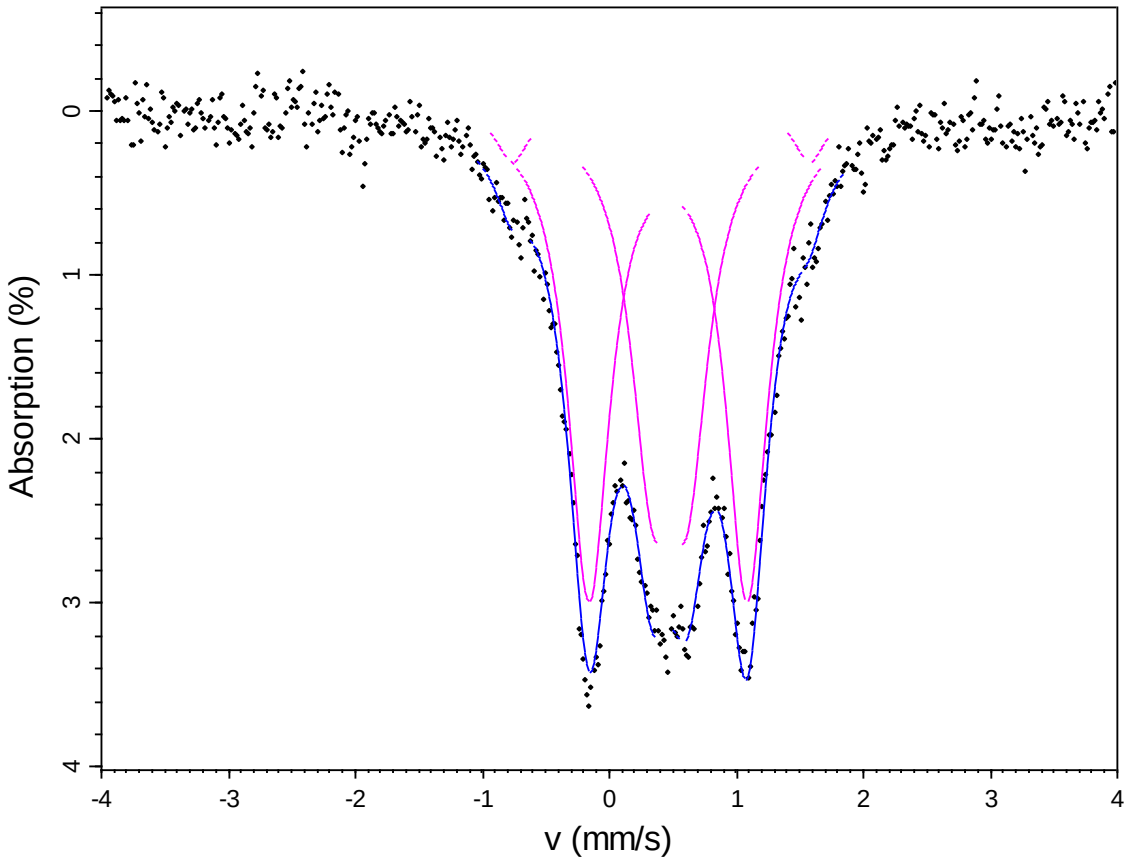

(c)

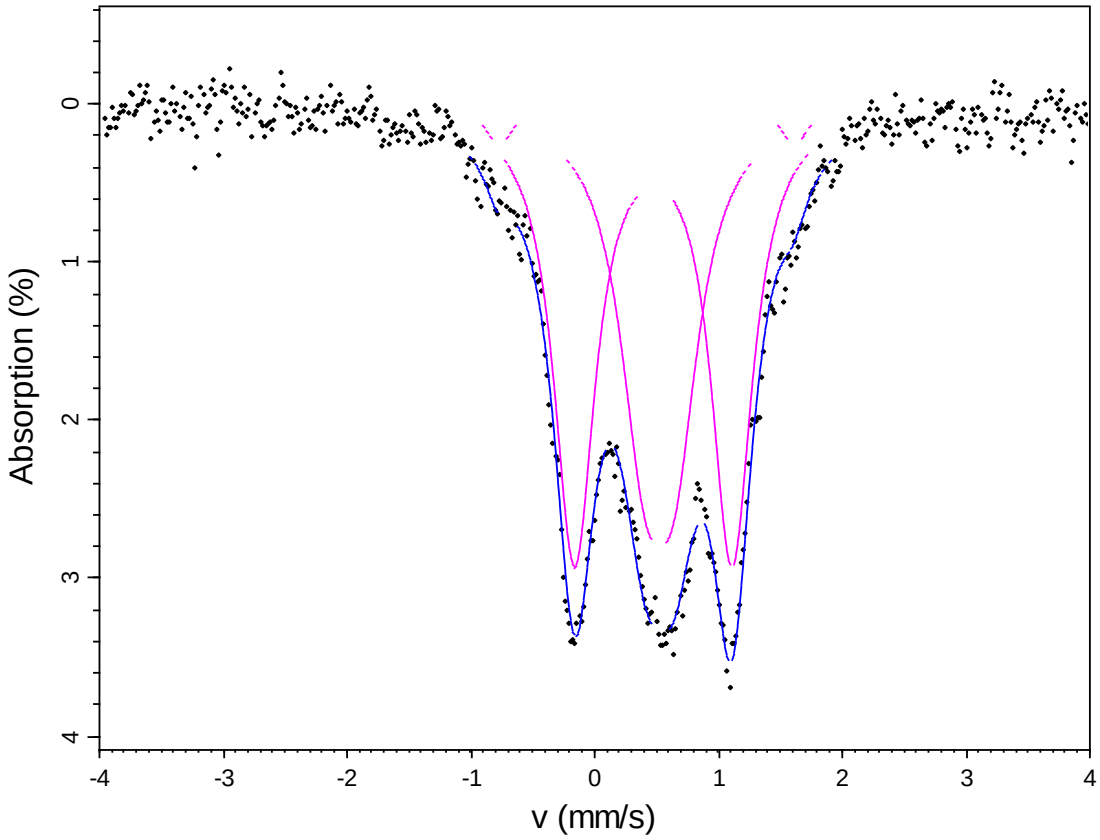

(d)

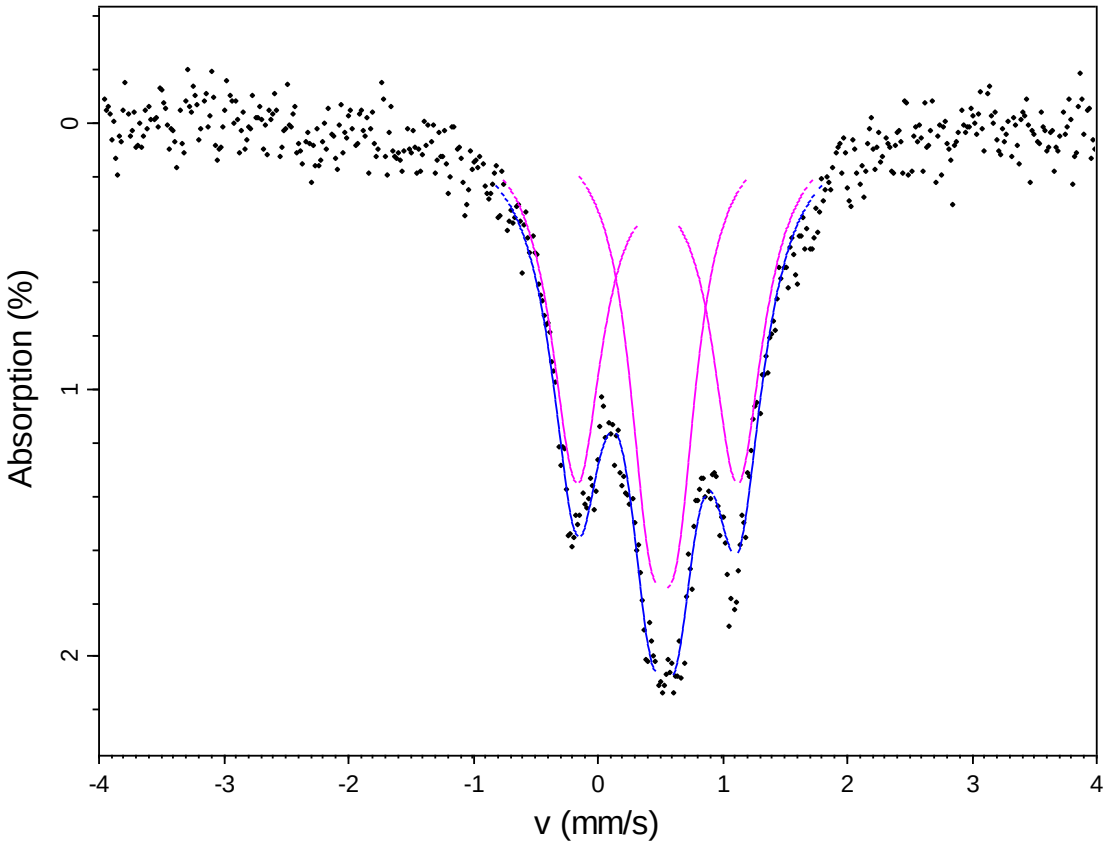

Figure S6. Fits to the room temperature Mössbauer spectra for the DP ferrates: **(a).** Sr_2FeTeO_6, **(b).** $Sr_2(Fe_{0.75}Ni_{0.25})TeO_6$, **(c).** $Sr_2(Fe_{0.5}Ni_{0.5})TeO_6$ and **(d)** $Sr_2(Fe_{0.25}Ni_{0.75})TeO_6$. The sharp and wide doublet reflects Fe *2a* site, while the narrow doublet with the appearance of a singlet reflects Fe *2d* site. The weak, broad doublet in the spectra of Sr_2FeTeO_6, $Sr_2Fe_{0.75}Ni_{0.25}TeO_6$ and $Sr_2Fe_{0.50}Ni_{0.50}TeO_6$ indicates the paramagnetic behavior of these samples.

7.6. Thermal analysis

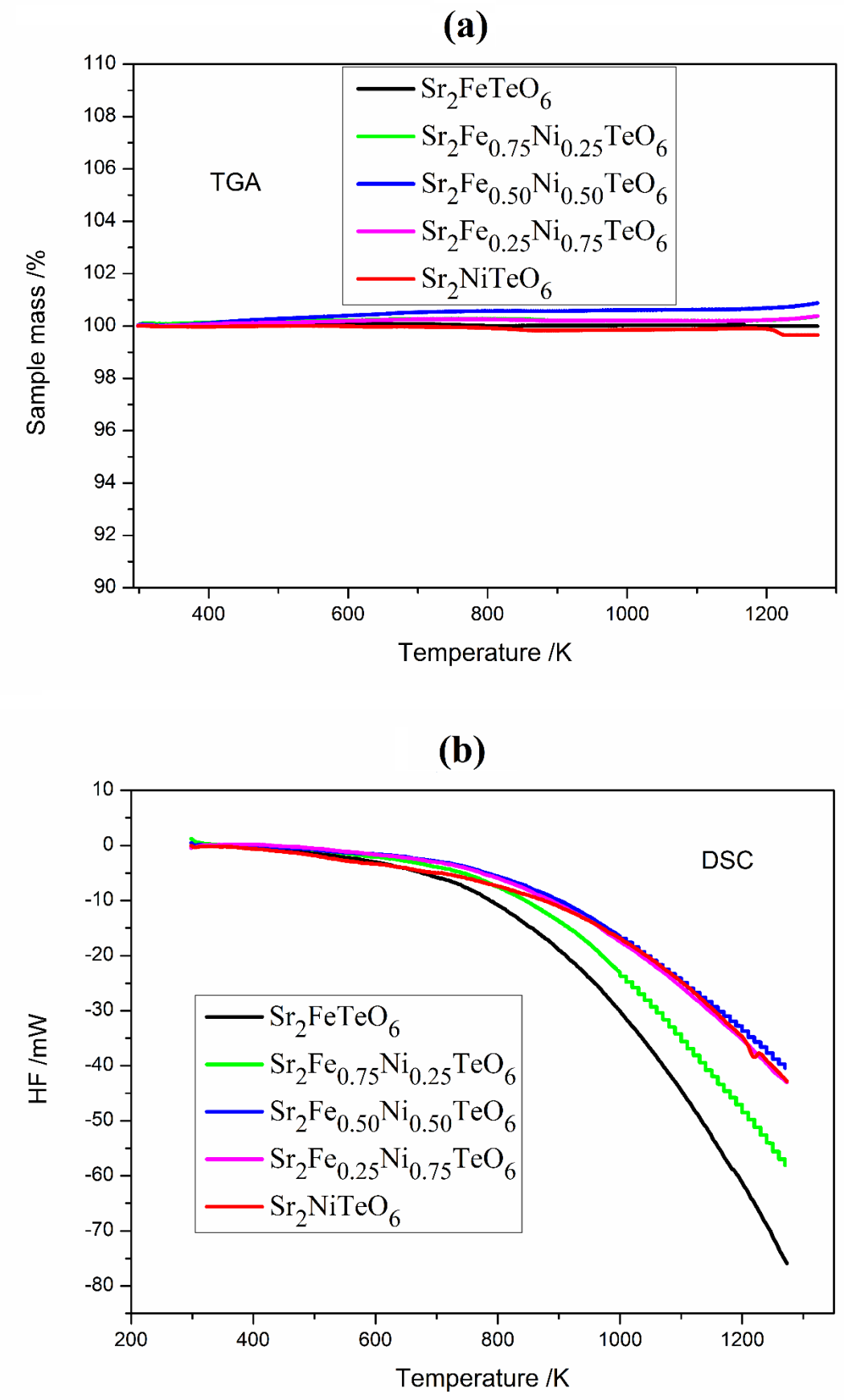

Figure S7. (a). TG and **(b).** DSC analysis of DP $Sr_2(Fe_{1-x}Ni_x)TeO_6$.

7.7. Magnetic properties

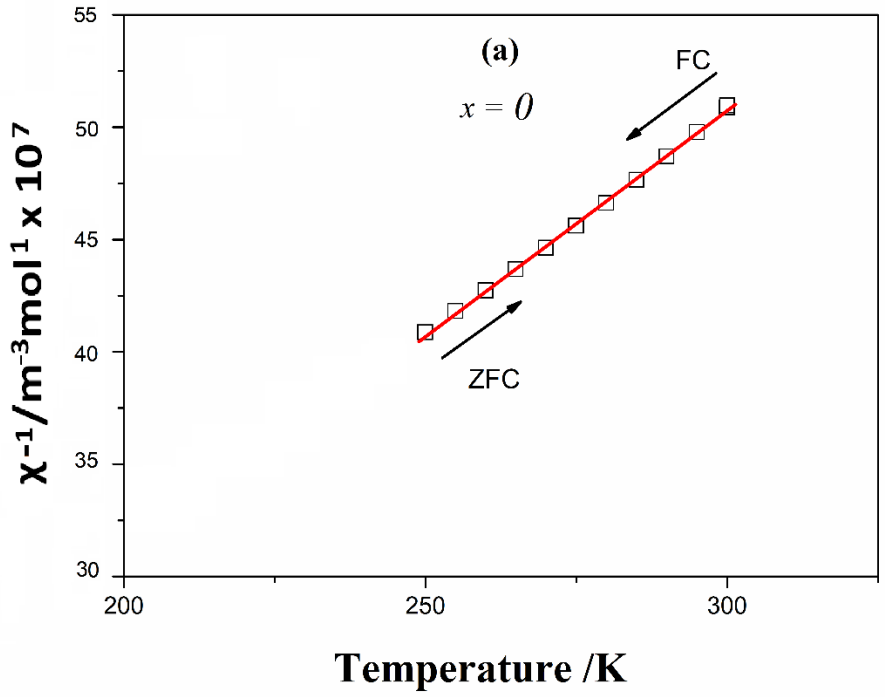

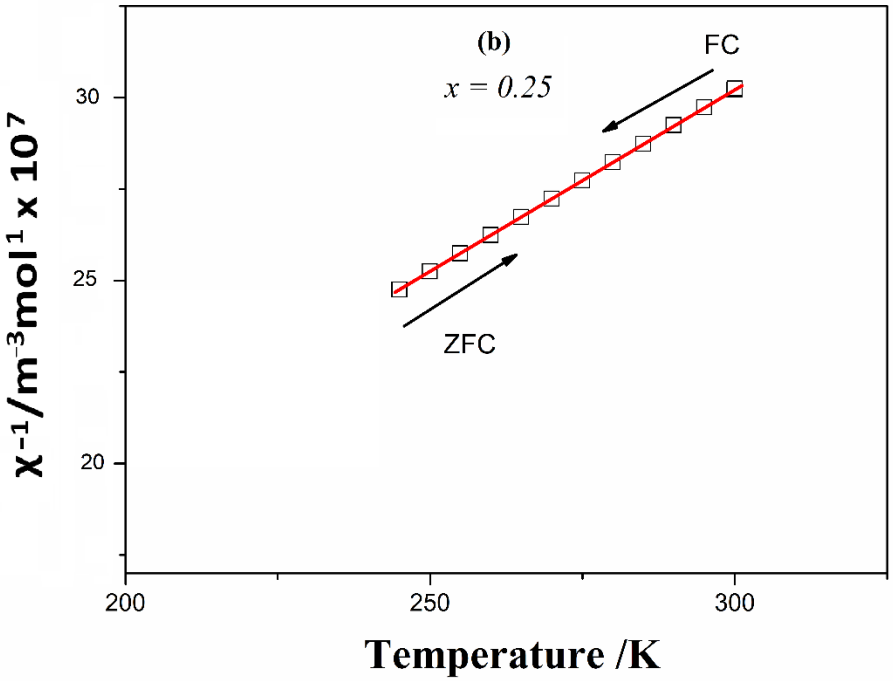

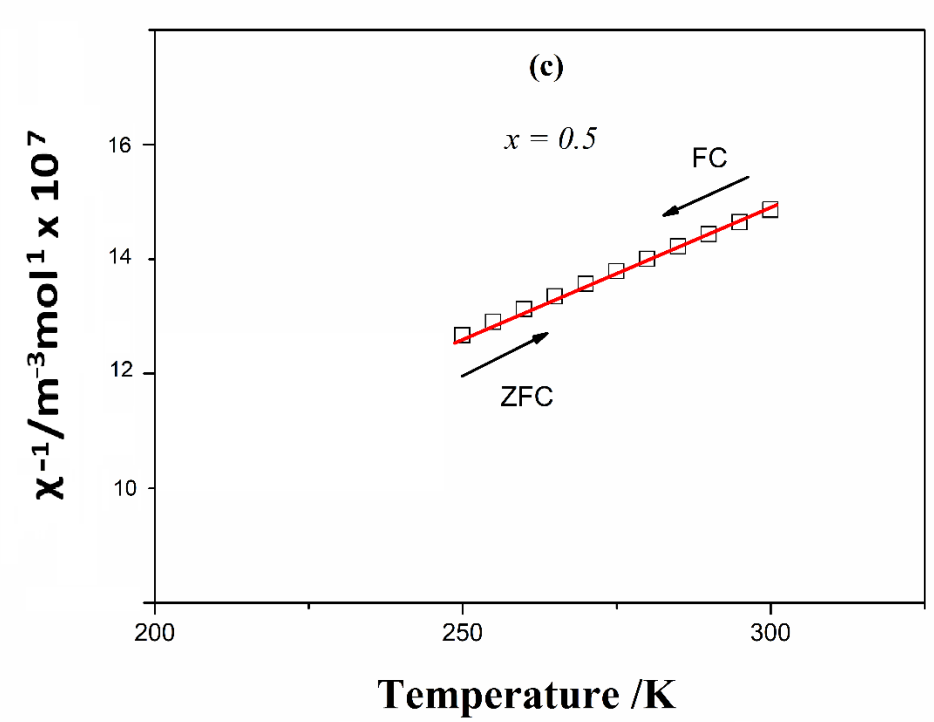
(c)
x = 0.5
FC
ZFC
16
14
12
10
200
250
300
χ-1/m-3mol1 x 107
Temperature /K

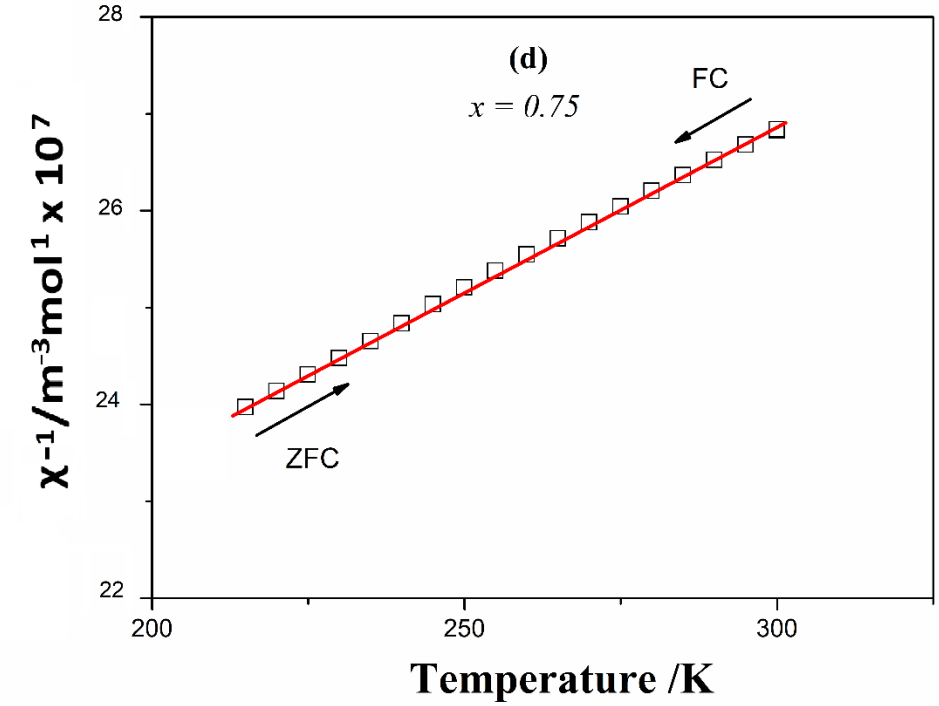
(d)
x = 0.75
FC
ZFC
28
26
24
22
200
250
300
χ-1/m-3mol1 x 107
Temperature /K

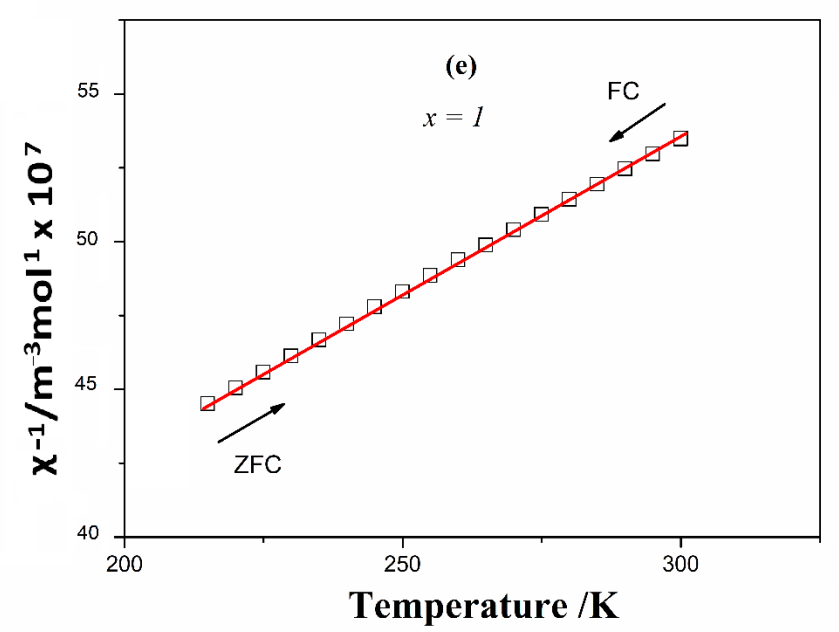

Figure S8. Inverse susceptibility of DP series: **(a)** Sr_2FeTeO_6, **(b)** $Sr_2(Fe_{0.75}Ni_{0.25})TeO_6$, **(c)** $Sr_2(Fe_{0.50}Ni_{0.50})TeO_6$, **(d)** $Sr_2(Fe_{0.25}Ni_{0.75})TeO_6$, and **(e)** Sr_2NiTeO_6.

Electronic supplementary information:

Experimental:

The Goldschmidt tolerance factor for a double perovskite, $A_2BB'O_6$ as follows:

$$t = \frac{r_A + r_O}{\sqrt{2}(\frac{r_B}{2} + \frac{r_{B'}}{2} + r_O)} \quad (1)$$

where r_A, r_B, $r_{B'}$, and r_O are the ionic radii as taken from Shannon [1] for the *A*, *B*, *B′* cations and oxygen anions, respectively. This parameter provides a measure of how well the *A*-site cations fits the twelve-fold (cubo-octahedral) coordination space within the corner-shared octahedral network formed by the *B*-site cations. It is well known that this tolerance factor depends on the size of ions located in *A* and *B* sites of double-perovskite structure. If the size of the *A* cation is greater than the size of the *B* cation, this factor is > 1. In contrast, $t < 1$ when the size of *A* cations is smaller than *B* cations. For $t = 1$ the structure is cubic [2].

The optical properties of the materials were studied by diffuse reflectance UV/Vis spectroscopy (DR-UV/Vis) with a Shimazdu, UV2600 spectrometer. Spectra were recorded over a wavelength range of 200 - 850 nm at room temperature. Barium sulfate was used as a standard. The band-gap energy was obtained from the reflectance spectra by employing Tauc's method [3] to transform the function:

$$\alpha(\frac{hc}{\lambda}) \approx B\,(\frac{hc}{\lambda} - E_g)^n \quad (2)$$

into the Kubelka - Munk function [4] to obtain the function *F(R)*, which is related to the absorption and scattering coefficients $k(\lambda)$ and $s(\lambda)$:

$$F(R) = \frac{[1-R(\lambda)]^2}{2R(\lambda)} = \frac{k(\lambda)}{s(\lambda)} \quad (3)$$

where *F(R)* is the Kubelka-Munk absorption, '*R*' is the diffuse reflectance, *h* is the Planck constant, *c* is the speed of light, λ is the wavelength of the impinging light, and E_g is the optical band gap in eV, *B* is a proportionality constant. The exponent n is the type of transition: n = 2 for indirect transitions, n = 1/2 for direct transitions [3 - 5]. Nevertheless, from such a treatment it can often be difficult to determine the nature of the optical transition and therefore an accurate band gap energy. An alternative is to apply a derivation of absorption spectrum fitting (DASF) [6] without knowing if the transition is direct or indirect, which is expressed by the following equation:

$$A(\lambda) = D\lambda\,(\frac{1}{\lambda} - \frac{1}{\lambda_g})^n \quad (4)$$

where $D = B(hc)^{n-1}z/2.303$, *z* is thickness of the reflecting layer, *A* is the absorbance at a wavelength λ, λ_g is the wavelength for corresponding band-gap energy. We can also use this Equation (3) in the followed form:

$$\frac{d[\ln(A(\lambda/\lambda)]}{d(1/\lambda)} = \frac{n}{(\frac{1}{\lambda} - \frac{1}{\lambda_g})} \quad (5)$$

In this method, the Kubulka-Munk function *F(R)* (equation 3) is assumed to be correlated to the absorption spectrum *A(λ)* [*A(λ) = F(R)*], that is by means of the scattering coefficient *s(λ)* which can be expressed as follow *s(λ) = s* (this coefficient can be independent of the wavelength). Consequently, the obtained data from the transformed reflectance of Kubelka-Munk function can be utilized to estimate transition wavelength [7].

The equation (5) helps to calculate the absolute value of band-gap energy E_g, which could be expressed by: $Eg = \frac{hc}{\lambda_g} = \frac{1239.81}{\lambda_g}$ $[eV]$ [8]. The idea is to get rid of the fixed transition exponent "n" by calculating the derivative of the absorption spectrum [8]. To its original successful use with thin films, this method was recently utilized for powders to determine the band gap energy [8]. The experimental work described herein demonstrates the possibility of employing the Reflectance-Absorption-Tauc-DASF (RATD) method [6], for deriving the transition types and band-gap energies of a series of isostructural compounds with varying composition.

References:

[1]. R. D. Shannon, *Acta Crystallogr.*, 1976, A32, 75.

[2]. Mailadil T. Sebastian, Dielectric Materials for Wireless Communication, 2008, 161-203.

[3]. J. Tauc, R.Grigorovici, A. Vancu, *Phys Status Solidi B*, 1966, 15:627–637.

[4]. P. Kubelka, and F. Munk, *Z Tech Phys*, 1931, 12:593–601.

[5]. R. Köferstein, L. Jäger, S. G. Ebbinghaus, *Solid State Ion.*, 2013, 249–250, 1–5.

[6]. D. Souri, Z. E. Tahan, *Appl Phys B*, 2015, 119:273–279.

[7]. M. Curti, A. Kirsch, L. I. Granone, F. Tarasi, G. López-Robledo, D.W. Bahnemann, M. M. Murshed, T. M. Gesing, and C. B. Mendive, *ACS Catal.*, 2018, 8, 9, 8844–8855.

[8]. K. Ghosh, M. M. Murshed, M. Fischer and T. M. Gesing, *J. Am. Ceram. Soc.*, 2022, 105, 1, 728-741.